SAPIENZA
UNIVERSITÀ DI ROMA

Facoltà di Ingegneria

Dottorato di Ricerca in Tecnologia Aeronautica e Spaziale
XXV ciclo

THE DETERMINATION OF THE HERMEAN GRAVITY AND TOPOGRAPHY FROM RADIO SCIENCE AND LASER ALTIMETER DATA OF THE MISSION BEPICOLOMBO

MANUELA MARABUCCI

RELATORE:
prof. Luciano Iess

A.A. 2011/2012

MANUELA MARABUCCI

THE DETERMINATION OF THE HERMEAN GRAVITY AND TOPOGRAPHY FROM RADIO SCIENCE AND LASER ALTIMETER DATA OF THE MISSION BEPICOLOMBO

Alla mia famiglia,
quella di sempre, di noi quattro
e quella nuova, di noi due

ACKNOWLEDGEMENTS

Grazie ai miei genitori e a mia sorella, che sono lì al mio fianco e partecipano ad ogni mio piccolo passo con amore e dedizione.

Grazie a Riccardo, che rende sempre tutto più facile con un sorriso o una risata.

Grazie a Sara, lontana ma vicinissima.

Grazie ai miei colleghi, che sanno mescolare bene il lavoro e il divertimento, la serietà e la confusione. Un grazie in più a Paolo, per il tempo che mi ha dedicato e la pazienza che ha dimostrato di avere.

Grazie al prof. Luciano Iess, per avermi dato la possibilità di lavorare nel suo team e di conoscere da vicino la realtà entusiasmante che sta dietro ad ogni missione spaziale.

Thanks to Prof. Dr. Tilman Spohn, Prof. Dr. Jürgen Oberst and Dr. Hauke Hußmann for hosting me at DLR in Berlin and for the interest shown in my work.

CONTENTS

LIST OF FIGURES

LIST OF TABLES

LIST OF ACRONYMS

AME Absolute Measurement Error

BELA BEpicolombo Laser Altimeter

DLR Deutsches zentrum für Luft-und Raumfahrt

DST Deep Space Transponder

ESA European Space Agency

FOV Field Of View

HGA High Gain Antenna

ISA Italian Spring Accelerometer

JAXA Japanese Aerospace Exploration Agency

JPL Jet Propulsion Laboratory

KAT Ka-band Transponder

LGA Low Gain Antenna

LOLA Lunar Orbiter Laser Altimeter

LRO Lunar Reconnaissance Orbiter

MESSENGER MErcury Surface, Space ENvironment, GEochemistry and Ranging

MGA Medium Gain Antenna

MGS Mars Global Surveyor

MMO Mercury Magnetospheric Orbiter

MOLA Mars Orbiter Laser Altimeter

MORE	Mercury Orbiter Radio science Experiment
MPO	Mercury Planetary Orbiter
MTM	Mercury Transfer Module
NAIF	Navigation and Ancillary Information Facility
NASA	National Aeronautics and Space Administration
OD	Orbit Determination
ODP	Orbit Determination Program
PFA	Probability of False Alarm
RMS	Root Mean Square
RFS	Radio Frequency System
RSE	Radio Science Experiment
SIMBIO-SYS	Spectrometers and Imagers for MPO BepiColombo Integrated Observatory System
SNR	Signal to Noise Ratio
SPICE	Spacecraft Planet Instrument C-matrix Events
TTC	Telemetry, Tracking and Command systems
TWTA	Travelling Wave Tube Amplifier
USN	Universal Space Network
WBRS	Wide Band Ranging System

INTRODUCTION

The synergy between the scientific instruments of a planetary probe has been always crucial to increase the scientific return of the mission. Different instruments may reveal the same feature or physical phenomenon, therefore providing a much stronger experimental evidence, or reveal the physical processes at play by resolving ambiguities associated to the data provided by a single instrument. These synergies are essential for the determination of the deep internal structure of planets and satellites, where one cannot count on seismic data as in the case of the Earth.

The geodesy and geophysics of planetary bodies is investigated by combining gravity, altimetry, rotation and, when available, magnetic field data. The methods and instruments of choice are precision Doppler tracking, laser or radio altimeters, high resolution imaging instruments (cameras or SAR), and magnetometers. Mars and the Moon are typical examples of bodies whose interior structure has been well determined thanks to a combination of gravity, topography and rotation (Neumann et al., 2004; Zuber et al., 2012).

The combination of different instruments and techniques has been profitably exploited also to increase the navigation accuracy of a space probe. For example, the combination of radio and optical data leads to large improvements in the relative positioning of a spacecraft with respect to an asteroid or a planet during flybys, or to the improvement of the ephemeris of the target body. In the orbital phases, radio tracking and laser altimetry has also been used for improved orbit determination and, ultimately, to a better determination of the body's gravity field.

The orbit determination (OD) is the first and essential step of space navigation. By combining a precise mathematical model of the spacecraft dynamics (also called dynamical model) and a set of observable quantities, such as range and range rate, the OD process provides the estimate of the spacecraft state vector at any given time. When, as it happens in most cases, some of the forces acting on the spacecraft are poorly known, the OD process produces also estimates of those forces through related parameters, such as the Stokes coefficients of the expansion of a planetary gravity field in spherical harmonics. De facto, the work of space geodesists and spacecraft navigators is largely overlapping. Most of the present knowledge on the planetary gravity fields and interior structures has been derived from accurate spacecraft tracking and precise orbit determination using the estimation theory methods.

In this work, the determination of the gravity field and topography of a planetary body is analyzed with specific reference to Mercury and the mission BepiColombo. The onboard instruments considered in this work are the Ka-band (32.3 - 34.0 GHz) transponder of the MORE investigation (MORE is the acronym of Mercury Orbiter Radio science Experiment), and the BepiColombo Laser Altimeter (BELA). The design and planning of the MORE geodesy measurements were supported by extensive numerical simulations, based upon the use of radio tracking data only. The analysis led to the assessment of the attainable accuracies in the reconstruction of the spacecraft orbit, the Hermean reference ellipsoid and "geoid".

It is however well known that other onboard instruments may contribute to the orbit reconstruction and therefore also to the gravity field determination, namely the laser altimeter and the high resolution camera. In particular, the use of laser altimetric observables has been successfully exploited in past missions to improve the orbital solutions (Lemoine et al., 2001; Mazarico et al., 2011). The question, whether altimetric observations can significantly contribute to the orbit determination of the Mercury orbiter, is therefore legitimate. Answering this question is the main goal of this work.

In literature, laser altimetric data have been used to provide the so called "crossover observables". Crossovers are points of the body's surface where laser ground tracks intersect. The corresponding observables used in the OD process are the differences between two laser altimeter measurements at the crossover points. It is therefore clear that an initial estimate of the spacecraft orbit is required in order to identify the crossovers. The accuracy of the crossover observables is limited by two main factors, namely the single shot precision of the laser system and the pointing accuracy of the spacecraft (quantified as the attitude absolute measurement error or AME). Generally, it is difficult to attain measurement accuracies better than 1 m.

Thanks to the adoption of an advanced radio system, based on Ka-band and multi-frequency links, and of an onboard accelerometer for the measurements of the spacecraft non-gravitational accelerations, it is expected that the orbital reconstruction of BepiColombo will be significantly more accurate than that of previous missions. The first objective of this thesis is to evaluate whether the next generation planetary orbiters, using advanced Ka-band tracking system, such as BepiColombo, may still benefit from the combination of radio and laser altimeter data in the orbit determination process. Crossover observables gave valuable contributions to the orbit determination, and therefore to the reconstruction of the topography, in the Lunar Reconnaissance Orbiter (LRO) mission (Mazarico et al., 2011). In that case, however, tracking data were provided by a much less accurate S-band radio system. Planetary orbiters using laser altimeters in combination with X-band radio systems, such as Mars Global Surveyor (MGS), also showed some improvements in the global orbital solution (Lemoine et al., 2001). However the benefits appear much more limited in this case, as the X-band radio data are significantly more stable than S-band data. Not surprisingly, this trend indicates that crossover contribution decreases when radio accuracy increases.

An additional goal is to devise the optimum strategy for the reconstruction of BepiColombo spacecraft orbit and the determination of the Hermean gravity field and topography, by choosing between a global fit with radio and crossover observables and a two steps approach, where the orbit is inferred only from tracking data and laser altimetric measurements are referenced to that orbit to obtain the topography of the planet. As the first approach is much more demanding from the computational point of view, it may be adopted only if there is a clear indication of significant benefits.

The thesis is organized as follows:

- **Chapter 1:** The importance of the scientific exploration of the planet Mercury, with a description of the past, current and future missions (Mariner 10, Messenger, BepiColombo);
- **Chapter 2:** The geodesy and radio science experiment of the mission BepiColombo, with a brief outline of the orbit determination process and the numerical simulations carried out so far;
- **Chapter 3:** The use of crossover observables in the orbit determination process, and the method used to simulate laser altimeter measurements, detect crossover location and include such observables in the simulations;
- **Chapter 4:** Numerical simulations of the geodesy experiment with and without the use of crossovers in the OD process, over-

all assessment of the estimation accuracy and efficiency for the different approaches, and suggestions for the optimal data analysis strategy to recover the spacecraft trajectory and the Hermean gravity field and topography.

Although the thesis considers the specific case of the ESA mission to Mercury, its main results can be applied, broadly speaking, to any planetary mission where laser altimetry is available in addition to radio tracking.

This work has been developed mainly at the Radio Science Laboratory of the Department of Mechanical and Aerospace Engineering, Sapienza University of Rome, in the context of the BepiColombo radio science experiment (MORE). Essential information on the operations and error models of laser altimeters was obtained during a three-months collaboration with the team of the BepiColombo laser altimeter (BELA), at DLR (Deutsches zentrum für Luft-und Raumfahrt) in Berlin.

1

MERCURY AND BEPICOLOMBO

1.1 SCIENTIFIC BACKGROUND

Mercury is an important target of planetary exploration in the Solar System. Difficult to view from Earth, due to its proximity to the Sun, it is even harder to reach by spacecraft, because of its location in the gravity well of the Sun and its challenging thermal environment. Departing from the Earth, a spacecraft needs to reduce energy to come closer to the Sun and, as the solar gravitational force increases with the square of the distance, the required reverse thrust increases accordingly. Furthermore, the thermal environment close to the Sun and to the hottest planet in the Solar System is extremely aggressive, with a direct solar radiation ten times higher than at the Earth's distance.

Nevertheless, Mercury holds answers to several critical questions regarding the formation and evolution of the terrestrial planets. These questions include the origin of Mercury's anomalous density, its high ratio of metal to silicate and its implications for planetary accretion processes, the nature of Mercury's geological evolution and interior cooling history, the mechanism of global magnetic field generation, the state of Mercury's core and the processes controlling volatile species in its polar deposits, exosphere and magnetosphere.

The density of Mercury does not conform with that of the other terrestrial planets, nor with that of the Moon. When corrected for compression due to the size, Mercury has the highest density of all. It has long been taken as evidence that iron is the most abundant contributor to the bulk composition. Several theories may account for this anomaly: the high solar-radiation levels may have reduced lighter oxides in Mercury to their heavier, metallic form; the heat of the Sun may have vaporized a large amount of Mercury's outer crust; or one or more gigantic impacts may have removed a substantial part of Mercury's rocky mantle, leaving a relatively large metallic core (Grard et al., 2000). By mapping the elements and minerals in Mercury's surface, it will be possible to establish which of these possibilities is likely. In addition, the core radius and density, the state of the core and the radius of a possible solid inner core can be addressed (Peale et al., 2002), by estimating libration rate and amplitude of rotation axis of the planet, its obliquity and the ratio between the moment of inertia of the solid outer layer and the moment of inertia of the entire planet (Peale, 2005).

Mercury is the only terrestrial planet, apart from the Earth, which has a significant magnetic field (equivalent to about one hundredth of that of the Earth (Grard et al., 2000)). However, little is known about the field characteristics. Mercury's magnetic field cannot be externally induced, on the grounds that the measured planetary field is far greater in magnitude than the interplanetary field. The dipole field could be a remanent or fossil field acquired during lithospheric cooling in the presence of an internal or external field, or it could be the product of a modern core dynamo.

As a result of Mercury's small dipole moment, the planet's magnetosphere is among the smallest in the Solar System. Although the magnetosphere shares many features with that of Earth, because of its small size the timescales for wave propagation and convective transport are much shorter at Mercury, and the proximity to the Sun renders the driving forces more intense. Strong variations in magnetic field and energetic particle characteristics observed by Mariner 10 have been interpreted as evidence of magnetic substorms and magnetic reconnection in the tail (Solomon et al., 2007).

Mercury's atmosphere is a surface-bounded exosphere whose composition and behavior are controlled by interactions with the magnetosphere and the surface. The exosphere is known to contain six element, but it is not stable on timescales comparable to the age of the planet, so there must be sources for each of the constituents. Proposed source processes for supplying exospheric species from Mercury's crust include diffusion from the interior, evaporation, sputtering by photons and energetic ions, chemical sputtering by protons, and meteoritic infall and vaporization (Solomon et al., 2007). That several of these processes play some role is suggested by the strong variations in exospheric characteristics observed as functions of local time, solar distance, and level of solar activity. The complex interactions among the solar wind, magnetosphere, exosphere, chemical composition, and interior may be clarified with dedicated space missions.

Global multicolor imaging of the surface from an orbiting spacecraft is required to make a substantial improvement in our knowledge of the full geological history of Mercury. Average resolution should be significantly better than that typical of Mariner 10 images, and a capability for targeted high-resolution imaging is desirable. MESSENGER is engaged in global imaging of Mercury's surface at a pixel dimension of about 250 m. As part of this mapping, targeted observations of selected areas are made using the Mercury Dual Imaging System (MDIS), with pixel dimensions of about 10 m for monochrome imaging and 80 m for multispectral images. Resolution is greatest - more than a factor of 10 better than with standard mapping - for areas northward of 20°N, where the spacecraft orbit is closest to Mercury. High-resolution images of Mercury's surface from orbit reveal that many bright deposits within impact craters exhibit fresh-appearing, irregular, shallow, rimless depressions. The depressions, or hollows, range from tens of meters to a few kilometers across, and many have high-reflectance interiors and halos. The host rocks, which are associated with crater central peaks, peak rings, floors, and walls, are interpreted to have been excavated from depth by the crater-forming process. The most likely formation mechanisms for the hollows involve recent loss of volatiles through some combination of sublimation, space weathering, outgassing, or pyroclastic volcanism. These features support the inference that Mercury's interior contains higher abundances of volatile materials than predicted by most scenarios for the formation of the solar system's innermost planet (Blewett et al., 2011).

Finally, among all bodies in the Solar System, Mercury is the best placed to probe the theory of gravitation since it experiences more than any other planet the gravity field of the Sun and moves with the highest velocity.

1.2 MERCURY'S EXPLORATION

For a long period, the only available data for studying Mercury were those collected by the NASA's mission Mariner 10 in 1973. With the launch of NASA Discovery class mission MESSENGER (MErcury Surface, Space ENvironment, GEochemistry and Ranging) in 2004, a new spacecraft is now orbiting around the planet, providing valuable information, while the incoming ESA and JAXA BepiColombo mission will reach Mercury in the 2022.

1.2.1 *Mariner 10*

Mariner 10 was the first mission to use a gravity assist with a planet, in order to reach another one. In the early 60's a UCLA graduate student, Micheal A. Minovitch, studied an interplanetary trajectory that allowed the spacecraft to reach Mercury, exploiting Venus gravity. Hence, an affordable Atlas/Centaur launch vehicle was sufficient to achieve one close approach to Venus and one to Mercury. In 1970, Dr. Giuseppe Colombo, of the Institute of Applied Mechanics in Padua, found the way to have two additional returns to Mercury, because the period of the spacecraft orbit would be two Mercury years, with spacecraft and Mercury arriving at the same point in the sky about six months after the first encounter (Shirley, 2003).

More than a decade of evolution of Mariner technology was exploited by the Mariner Venus-Mercury 1973 spacecraft, which was the sixth of a series that began with Mariner Venus in 1962 and included Mariner Mars 1964, Mariner Venus 1967, Mariner Mars 1969 and Mariner Mars Orbiter 1971. In common with earlier spacecraft, Mariner 10 used an octagonal main structure, solar cells and a battery for electrical power, three-axis attitude stabilization and control by nitrogen gas jets, celestial references by star and Sun sensors, S-band radio for command, telemetry, and ranging, a high-gain antenna, a low-gain antenna, a scan platform to point science instruments, and a hydrazine rocket propulsion system for trajectory corrections.

Some changes to the Mariner concept were needed for the mission to Mercury, principally because the spacecraft had to approach the Sun much closer than any previous planetary spacecraft. This required improved ways to insulate the spacecraft from solar radiation. Thermal control required, in addition to a large sunshade, louvers and protective thermal blankets, and the ability to rotate the solar panels about their axis, in order to keep the cells at a suitable temperature. Other major design changes from past Mariners included the use of a larger data rate and the capability for both S- and X-band ranging and X-band carrier transmission. In addition, the new Mariner had a central articulation and pointing subsystem for its scan platform, its two-degree-of-freedom high-gain antenna, and its tillable solar panels, with either closed-loop positioning or discrete incremental command capability. Finally, the propulsion system had to be capable of multiple firings, in order to accommodate the number of in-flight trajectory correction maneuvers required for precise navigation.

Before Mariner 10, little was known about Mercury, so to provide the greatest amount of information obtainable with remote sensing devices, Mariner Venus-Mercury carried more science instruments

Mariner 10 payload
Television Photography The equipment consisted of two spherical Cassegrain telescopes with eight filters, each attached to a vidicon tube camera for narrow-angle photography, plus an auxiliary optical system providing wide-angle photography. The objectives were to photograph Venus upper atmosphere and Mercury's surface,to determine its spin axis and to establish a cartographic coordinate system.
Celestial Mechanics and Radio Science The onboard radio system allowed to have radio observables in X- and S- band. Tracking information was analyzed to determine mass and gravitational characteristics of both Venus and Mercury, while the occultations were used to study the signals during spacecraft passage through the planetary atmospheres, in order to compute temperature and pressure profiles for the atmospheric composition models.
Scanning Electrostatic Analyzer and Electron Spectrometer The instrumentation consisted of two sunward-facing electrostatic analyzers and one backward facing electron spectrometer, mounted on a scanning platform. This plasma experiment was designed to analyze of interaction between the planet Mercury and the solar wind, to study the plasma regime at Mercury, to verify and extend previous observations of the solar wind interaction with Venus, and to study the solar wind between 0.4 and 1 AU.
Triaxial Fluxgate Magnetometer This experiment consisted of two triaxial fluxgate magnetometers mounted on a common boom, 2.3 m and 5.8 m from the spacecraft, and designed to measure the vector magnetic field in the vicinity of Mercury and Venus and in the interplanetary medium. Outputs from the two magnetometers were simultaneously analyzed to separate ambient fields from spacecraft fields.
Extreme Ultraviolet Spectrometer The extreme ultraviolet spectrometer consisted of two instruments: an occultation spectrometer (body-fixed) and an airglow spectrometer (mounted on the scan platform). When the sun was obscured by the limbs of the planet, the occultation spectrometer measured the extinction properties of the atmosphere. The airglow spectrometer was flown measured airglow radiation from Venus and Mercury in the spectral range from 20 to 170 nm.
Two-Channel Infrared Radiometer The infrared radiometer utilized two channels, (22 - 39 µm and 10 - 17 µm), to observe the thermal emission from Venus and Mercury. The infrared thermal emission from the surface of Mercury between late afternoon and early morning (local time) and deviations from the average thermal behavior of the surface were measured. Measurements were also made of the brightness temperatures of Cytherian cloud tops and limb darkening phenomena.
Energetic Particles Experiment This experiment was designed to measure energetic electrons, protons, and alpha particles in the interplanetary medium and in the vicinities of Venus and Mercury. The instrumentation consisted of a main telescope and a low-energy telescope. The main telescope was formed by six co-linear sensors surrounded by a plastic scintillator anti-coincidence cup.

Table 1.1: Short description of Mariner 10's scientific instrumentation

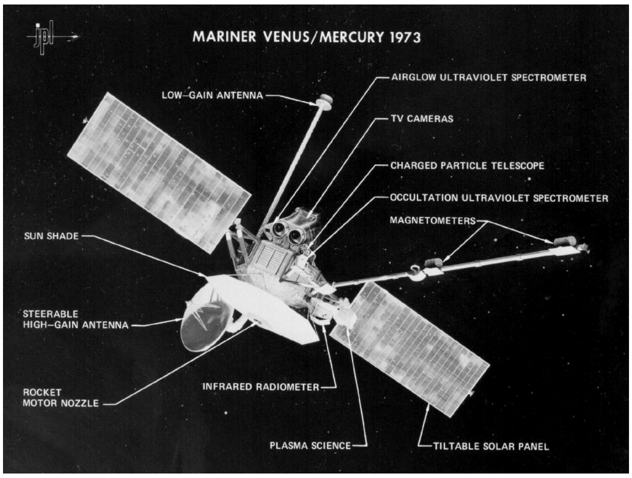

Figure 1.1: Mariner 10's payload

than most previous Mariner spacecraft (figure 1.1 and table 1.1 [1]). A magnetometer measured magnetic fields, a plasma analyzer measured the ions and electrons of the solar wind, and cosmic ray telescopes provided information on solar and galactic cosmic rays. The main objective of these instruments was to learn about the planet by studying its effects on the interplanetary medium. An infrared radiometer measured temperatures of the clouds of Venus and the surface of Mercury. Two independent ultraviolet instruments analyzed the planetary atmospheres. One instrument was fixed to the body of the spacecraft and was used at Mercury to search for traces of atmosphere along the edges of the visible disc of the planet. A second instrument, mounted along with the television cameras on a scan platform, could be pointed on command. This spectrometer was used to scan both the planets, searching for evidence of hydrogen, helium, argon, neon, oxygen, and carbon. At Venus, it searched for specific gases, and during the cruise phase it looked for sources of ultraviolet radiation coming from hot stars and gas clouds in the galaxy. Measurements were also made of the gaseous envelope surrounding the comet Kohoutek. A complex of two televisor cameras with eight filters was the basis of the imaging experiment. These cameras were capable of taking both narrow- and wide-angle views of Venus and Mercury. Sharing the scan platform with the spectrometer, the imaging complex was directed by command from Earth. As well as taking pictures in different colors of light, these cameras also measured how the light was polarized, observations intended to provide information on the composition of the clouds of Venus and the surface of Mercury.

---

[1] http://nssdc.gsfc.nasa.gov/nmc/experimentSearch.do?spacecraft=Mariner%2010

A radio experiment used the signals transmitted from the spacecraft to Earth. By tracking the spacecraft signals, it is possible to determined how the spacecraft is affected by the gravitational fields of the planets and the gravitational field itself can be recovered. By analysis of the radio signals passed close to the limb or edge of the planet, the atmosphere of Venus was studied and the existence of Mercury's atmosphere was checked (Dunne and Burgess, 1978).

Mariner 10 suffered a number of failures (problems with the gyro-system, the high gain antenna, the star tracker, the protective door of the plasma science experiment, the heaters for the TV cameras...) but anyway the results exceeded the expectations (Dunne and Burgess, 1978). Mariner 10 gave an invaluable contribution to our knowledge of Mercury. It discovered a weak magnetic field, that was not expected because of Mercury's small size and slow rotation. Mariner 10 detected also an atmosphere, mainly composed by helium and provided clues about the iron core. About 40 - 45% of the surface was covered by images and a complete mapping of six out of fifteen quadrants was carried out, showing huge craters basins (Burgess, 1974).

Only eight days after the third encounter with Mercury, Mariner 10's supply of attitude control gas was finally exhausted and the spacecraft's radio transmitter was turned off, leaving a silent spacecraft orbiting the Sun.

1.2.2 *MESSENGER*

The MErcury Surface, Space ENvironment, GEochemistry and Ranging (MESSENGER) spacecraft, launched on August 2004 is the first probe to orbit Mercury. It is part of the Discovery Program of the U.S. National Aeronautics and Space Administration (NASA).

The mission MESSENGER has been designed to address six key scientific questions:

- what planetary formation processes led to the high metal/silicate ratio in Mercury?
- what is the geological history of Mercury?
- what are the nature and origin of Mercury's magnetic field?
- what are the structure and the state of Mercury's core?
- what are the radar-reflective materials at Mercury's poles?
- what are the important volatile species and their sources and sinks on and near Mercury?

The answer to these questions bears not only on the nature of the planet, but also more generally on the origin and comparative evolution of all the terrestrial planets. Indeed, a substantially improved knowledge of Mercury is critical to our understanding of how terrestrial planets formed and evolved. Determining the surface composition of Mercury, a body with a ratio of metal to silicate higher than any other planet or satellite, will provide a unique window on the processes by which planetesimal in the primitive solar nebula accreted to form planets. Documenting the global geological history will elucidate the role of planet size as a governor of magmatic and tectonic history for a terrestrial planet. Characterizing the nature of the magnetic field of Mercury and the size and state of Mercury's core will allow us to generalize our understanding of the energetics and lifetimes of magnetic dynamos, as well as core and mantle thermal histories, in solid planets and satellites. Determining the nature of volatile species in Mercury's polar deposits, atmosphere, and magnetosphere will provide critical insight into volatile inventories, sources, and sinks in the inner Solar System (Solomon et al., 2001).

The selection of MESSENGER as a NASA Discovery Program mission was a decision rooted in a 25-year history of Mercury exploration and strategic planning for improving our understanding of the inner planets. Immediately following the Mariner 10 mission, a Mercury orbiter was widely recognized as the obvious next step in the exploration of the planet. In the late 1970s, however, it was thought that the change in spacecraft velocity required for orbit insertion around Mercury was too large for conventional propulsion systems. In the mid-1980s, about a decade after the end of the Mariner 10 mission, multiple gravity-assist trajectories were discovered that could achieve Mercury orbit insertion with chemical propulsion systems. This finding stimulated detailed studies of Mercury orbiter missions in Europe and the United States between the mid-1980s and early 1990s. During the same time interval there were important discoveries made by ground-based astronomy.

In the early 1990s, after re-examining its approach to planetary exploration, NASA initiated the Discovery Program, intended to foster more frequent launches of less costly, and more focused missions selected on the basis of rigorous scientific and technical competition. Mercury was the target of a number of early unsuccessful proposals to the Discovery Program for flyby and orbiter missions. The MESSENGER concept was initially proposed to the NASA Discovery Program in 1996, and after multiple rounds of evaluation the mission was selected for flight in July 1999 (Solomon et al., 2007).

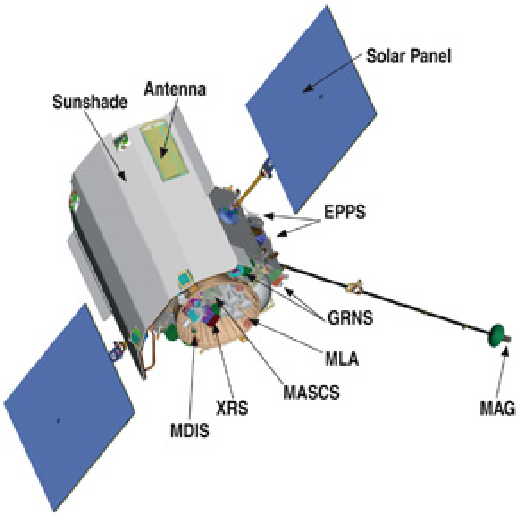

Figure 1.2: MESSENGER's payload

The spacecraft is three-axis stabilized and momentum biased to ensure Sun pointing while allowing instrument viewing by rotation about the spacecraft - Sun line. Power is provided by two specially designed solar arrays consisting of two-thirds mirrors and one-third solar cells for thermal management and, because the spacecraft is solar powered (except for a battery needed for eclipses), power generation increases as the spacecraft moves sunward. Generally passive thermal management techniques have been used on the rest of the spacecraft to minimize the required power while protecting the spacecraft from the harsh environment near the Mercury dayside. Telecommunications are provided by redundant transponders, solid-state power amplifiers, and a diverse antenna suite that includes two phased-array antennas, the first electronically steered antennas designed for use in deep space.

The key questions lead to a set of seven miniaturized scientific instruments, plus the spacecraft communication system (see figure 1.2 and table 1.2[2]). Onboard there is a dual imaging system for wide and narrow field of view, monochrome and color imaging, and stereo; γ-ray, neutron, and X-ray spectrometers for surface chemical mapping; a magnetometer; a laser altimeter; a combined UV-visible and visible-near-infrared spectrometer to survey both exospheric species and surface mineralogy; and a combined energetic particle and plasma spectrometer to sample charged species in the magnetosphere.

MESSENGER was launched successfully by a Delta II 7925H-9.5 rocket on August 3, 2004. The cruise phase of the mission was 6.6 years

---

[2] http://www.nasa.gov/mission_pages/messenger/spacecraft/index.html

MESSENGER payload
Mercury Dual Imaging System (MDIS) This instrument consists of wide-angle and narrow-angle imagers that will take pictures of Mercury in visible and near-infrared light, allowing to map landforms, track variations in surface spectra and gather topographic information. A pivot platform will help point it in whatever desired direction.
Gamma-Ray and Neutron Spectrometer (GRNS) This instrument will detect γ rays and neutrons that are emitted by radioactive elements on Mercury's surface or by surface elements that have been stimulated by cosmic rays. It will be used to map the relative abundances of different elements and will help to determine if there is ice at Mercury's poles, which are never exposed to direct sunlight.
X-Ray Spectrometer (XRS) γ rays and high-energy X-rays from the Sun, striking Mercury's surface, can cause the surface elements to emit low-energy X-rays. XRS will detect these emitted X-rays to measure the abundances of various elements in the materials of Mercury's crust. XRS data will be used to create a map of which elements are present on the planet's surface, allowing a characterization of Mercury's chemical composition and geologic history.
Magnetometer (MAG) This instrument is at the end of a 3.6 m boom, that keeps it away from the spacecraft's own magnetic field. The sensor, protected by its own sunshade, will map Mercury's magnetic field and will search for regions of magnetized rocks in the crust, obtaining crucial information for determining its source.
Mercury Laser Altimeter (MLA) MLA maps Mercury's landforms and other surface characteristics using an infrared laser transmitter and a receiver that measures the round-trip time of individual laser pulses. The data will also be used to track the planet's slight, forced libration, which can contribute to the determination of the state of Mercury's core.
Mercury Atmospheric and Surface Composition Spectrometer (MASCS) Combining an ultraviolet spectrometer and infrared spectrograph, MASCS will measure the abundance of atmospheric gases around Mercury and detect minerals in its surface materials. These measurements are needed to understand the processes that generate and maintain the exosphere, the connection between surface and atmospheric composition, and the nature of the radar-reflective materials near the planet's poles.
Energetic Particle and Plasma Spectrometer (EPPS) EPPS will measure the mix and characteristics of charged particles in and around Mercury's magnetosphere using an Energetic Particle Spectrometer (EPS) and a Fast Imaging Plasma Spectrometer (FIPS). Both are equipped with time-of-flight and energy-measurement technologies to determine simultaneously particle velocities and elemental species.
Radio Science (RS) RS will use the Doppler effect to measure very slight changes in the spacecraft's velocity as it orbits Mercury. This allows studying Mercury's gravity field and mass distribution, and supporting the laser altimeter investigation to determine the size and condition of Mercury's core.

Table 1.2: Short description of MESSENGER's scientific instrumentation

in duration and included six planetary flybys (one of Earth, two of Venus, and three of Mercury) as well as a number of propulsive corrections to the trajectory. At the spacecraft's fourth encounter with Mercury, orbit insertion was accomplished on March 18, 2011. Few days after the orbit insertion, the spacecraft was placed in its mapping orbit, which has an 80° inclination to Mercury's equator, an initial 200 km minimum altitude over 60°N latitude, and a 12 h orbit period. As a result of solar torques, the periapsis latitude drifts northward and the minimum altitude progressively increases. Once per 88 days Mercury's year the spacecraft executed orbit correction maneuvers to return the minimum altitude to 200 km. Other propulsive events had been minimized to permit the recovery of Mercury's gravity field from ranging and Doppler velocity measurements: the dynamical coherence of the spacecraft trajectory is a fundamental requirement for the arc devoted to gravity experiments.

1.2.3 *BepiColombo*

BepiColombo is a planetary Cornerstone of ESA's Cosmic Vision Programme, devoted to the exploration of Mercury and its environment. BepiColombo is a dual spacecraft mission, jointly carried out by ESA (European Space Agency) and JAXA (Japanese Aerospace Exploration Agency).

The scientific background and the main scientific objectives, as outlined in Benkhoff et al. (2010) and Grard and Balogh (2001) are:

- origin and evolution of Mercury, the closest planet to our parent star;
- Mercury's figure, including mean radius, polar radius and equatorial radius, interior structure and composition;
- interior dynamics and origin of its magnetic field
- exogenic and endogenic surface modifications, cratering, tectonics and volcanism;
- composition, origin an dynamics of Mercury's exosphere and polar deposit;
- structure and dynamics of Mercury's magnetosphere;
- test of Einstein's theory of general relativity.

A Mercury mission was first proposed in 1993 and following several investigation by ESA; the BepiColombo mission was selected as the 5th cornerstone mission of the Horizon 2000 science programme. At the beginning, the limited lift-off capability required very lightweight solution and therefore, clever mission scenario and technology developments in order to survive to the harsh thermal and radiation environments around Mercury. During the definition phase the preliminary design was consolidated and critical technology was developed. The mission was approved as part of the Cosmic Vision programme in the 2007. In 2008, a severe mass crisis came up, due to negative and unexpected test results on mission essential technologies. This event caused a redesign of the spacecraft, with larger area for the solar panels, a more robust structure and more fuel consumption, necessitating also a change of the launch vehicle from the baselined Soyouz-Fregat to Ariane 5 (Benkhoff et al., 2010).

The first spacecraft, the MPO (Mercury Planetary Orbiter), led by ESA, will focus on a global characterization of Mercury through the investigation of its interior, surface, exosphere and magnetosphere, thanks to the eleven onboard instruments: cameras, spectrometers (IR, UV, X-ray, γ-ray, neutron), radiometer, laser altimeter, magnetometer, particle analyzer, Ka-band transponder and accelerometer (see table 1.3[3]). The second spacecraft, the MMO (Mercury Magnetospheric Orbiter), under the responsibility of JAXA, will carry five instruments to study the environment around Mercury (see table 1.4[4]), including the planet's exosphere and magnetosphere, and their interaction processes with the solar wind and the planet itself (magnetometer, ion spectrometer, electron energy analyser, cold and energetic plasma detectors, plasma wave analyzer, and imager).

The two spacecrafts will be launched in a composite with a propulsion element, the Mercury Transfer Module (MTM). It provides the acceleration and braking required during the cruise, to reach Mercury. The launch is now foreseen for August 2015. After one year, the spacecraft comes back to the Earth and is deflected towards Venus. Two consecutive Venus flybys reduce the perihelion to nearly Mercury distance. A sequence of four Mercury flybys lower the relative velocity and four final thrust arcs further reduce it, such that the spacecraft will be weakly captured by Mercury on January 2022. After the approach through the weak stability boundary of the planet, the spacecraft needs only a small velocity change for a firm capture. The insertion manoeuvres are performed by the chemical propulsion engines, embedded in the MPO. Once the MMO orbit is reached, the MMO is released and the MMO Sunshield and Interface Structure (MOSIF) is jettisoned. An additional thrust phase will insert the MPO

---

[3] `http://sci.esa.int/science-e/www/object/index.cfm?fobjectid=38831`

[4] `http://sci.esa.int/science-e/www/object/index.cfm?fobjectid=38832`

into its final orbit, lowering the apocenter and rotating the line of apsides. The baselined timelife of the MPO and MMO in Mercury orbit is one terrestrial year, but a mission extension by another year is foreseen Jehn (2012).

BepiColombo MPO payload

BepiColombo Laser Altimeter (BELA)

BELA is a laser altimeter based on the classical principle of laser pulse time of flight measurement and it aims to measure the figure axes of the planet to 10 m accuracy and the topography with a single-shot ranging accuracy of 1 m and with a grid spacing of a few hundred meters along-track. In addition, the tidal deformation and libration of the planet will be deduced from the longterm datasets.

Italian Spring Accelerometer (ISA)

The three-axis high sensitive accelerometer will measure the inertial acceleration acting on the MPO. Such data, together with tracking data are used to evaluate the purely gravitational trajectory of the MPO, transforming it to a virtual drag-free satellite system.

Mercury Magnetometer (MERMAG)

The primary objective of the MPO Magnetometer is to collect magnetic field measurements in order to describe Mercury's planetary magnetic field and its source in great detail, also supported by similar measurements made on MMO. The secondary objectives are related to the interaction of the solar wind with Mercury's magnetic field and the planet itself.

Mercury Thermal Infrared Spectrometer (MERTIS-TIS)

MERTIS is an IR-imaging spectrometer, with the goal of providing detailed information about the mineralogical composition of Mercury's surface layer by globally mapping spectral emittance with a high-spectral resolution. In addition MERTIS will be able to measure thermo physical properties of the surface, like thermal inertia and surface texture.

Mercury Gamma ray and Neutron Spectrometer (MGNS)

The scientific goals are to measure the elemental surface and subsurface composition over the entire surface of Mercury by measuring the nuclear lines of major soil-composing elements, the leakage flux of neutrons and the lines of natural radioactive elements.It will also determine the regional distribution of volatile depositions on the polar areas of Mercury, and provide a map of column density of these depositions

Mercury Imaging X-ray Spectrometer (MIXS)

MIXS is designed to perform X-ray fluorescence (XRF) analysis of the surface of Mercury. XRF is a well-known technique used for remote sensing the atomic composition of airless, inner solar system bodies. The interpretation of the MIXS measurements requires the knowledge of the solar X-ray flux monitored by the SIXS experiment.

Mercury Orbiter Radio science Experiment (MORE)

Continuing in the next page

Continued from the previous page

BepiColombo MPO payload
MORE will determine the gravity field of Mercury as well as the size and physical state of its core. It will provide crucial experimental constraints to models of the planet's internal structure and test theories of gravity with unprecedented accuracy, exploiting the performances of a novel tracking system (with X-X, X-Ka and Ka-Ka links) and precise orbit determination.
Probing of Hermean Exosphere by Ultraviolet Spectroscopy (PHEBUS) PHEBUS is a UV spectrometer devoted to the characterization of Mercury's exosphere, in terms of structure, composition and dynamics and to the understanding of the coupled surface-exosphere-magnetosphere system. The spectral range of PHEBUS contains the major resonance lines of most expected or detected species.
Search for Exosphere Refilling and Emitted Neutral Abundances (SERENA) SERENA will provide information about the global surface-exosphere-magnetosphere system and its interaction with the solar wind. The experiment consists of four sensors that can be operated individually: Emitted Low-Energy Neutral Atoms(ELENA, measuring energetic neutral particles), Start from a Rotating Field Mass Spectrometer (STROFIO, a neutral particle spectrometer), Miniature Ion Precipitation Analyser (MIPA, an ion spectrometer), and Planetary Ion Camera (PICAM, an ion mass spectrometer).
Spectrometers and Imagers for MPO BepiColombo Integrated Observatory System (SIMBIO-SYS) This instrument suite is an integrated package for the imaging and spectroscopic investigation of the surface of Mercury. The science goals are to examine the surface geology, volcanism, global tectonics, surface age, surface composition, and geophysics of Mercury. It incorporates capabilities to perform medium-spatial resolution global mapping in stereo and color imaging using two pan-chromatic and three broad-band filters, respectively, as well as high-spatial resolution imaging with pan-chromatic and three broad-band filters and imaging spectroscopy in the spectral range 400Ð2000 nm.
Solar Intensity X-ray Spectrometer (SIXS) SIXS will monitor solar X-rays (SIXS-X) and energetic particles (SIX-P). The X-ray data are mandatory for a fluorescence analysis of MIXS spectra. Scientific objectives for SIXS-X are to monitor the solar X-ray corona and solar flares and to determine their temporal variability and spectral classification. SIXS-P will monitor solar energetic electron and proton fluxes and their variabilities. The key scientific objective is to study the interaction of this radiation with MercuryÕs exosphere, magnetosphere and surface.

Concluded from previous page

Table 1.3: Short description of BepiColombo MPO's scientific instrumentation

The choice of MPO and MMO orbits (see figure 1.3) is mainly a compromise between science objectives and thermal load on the spacecraft. Scientific instruments require global, high-resolution coverage, implying a polar orbit at low altitude. On the other side, the

BepiColombo MMO payload
Mercury Magnetometer (MERMAG-M/MGF) TheMMO/MAG consists of two sets of fluxgate magnetometers, MGF-O for the outer sensor and MGF-I for the inner sensor (where MGF-O is a so- called digital-type and MGF-I is a traditional analogue-type). The primary objective of the MMO Magnetometer is to collect magnetic field measurements.
Mercury Plasma Particle Experiment (MPPE) MPPE is a comprehensive instrument package for plasma, high energy particle and energetic neutral atom measurements. It consists of seven sensors. Six of them perform in-situ observations and cover the particle species and the energy range of interest from the space plasma physics point of view. Meanwhile the last one will detect energetic neutrals created via charge-exchange and will provide remote information on how plasma and neutral gas interacts in the Hermean environment.
Plasma Wave Instrument (PWI) PWI will provide the first electric field, plasma waves, and radio waves data from the Mercury plasma environment. It will give important information regarding energy exchange processes in the small magnetosphere where the role of micro-physics is more visible than any where else. The PWI consists of three receivers, connected to two sets of electric field sensors and two kinds of magnetic field sensors.
Mercury Sodium Atmospheric Spectral Imager (MSASI) Direct exposure of Mercury's rocky surface to the space environment gives the planet distinct characteristics in its atmospheric composition. Its tenuous atmosphere is known to have substantial sodium component. MSASI is a high-dispersion visible spectrometer working in the spectral range around sodium D2 emission (589 nm).
Mercury Dust Monitor (MDM) The main objective of MDM is to clarify the dust environment at Mercury's region of the solar system. The impact of micro-meteoroids may contribute significantly as one of the source processes of the planetÕs tenuous atmosphere. At Mercury's position, the main components of dust particles are Keplerian dust particles and beta-meteoroid particles. This instrument can detect impact momentum, crude direction and the number density of the dust.

Table 1.4: Short description of BepiColombo MMO's scientific instrumentation

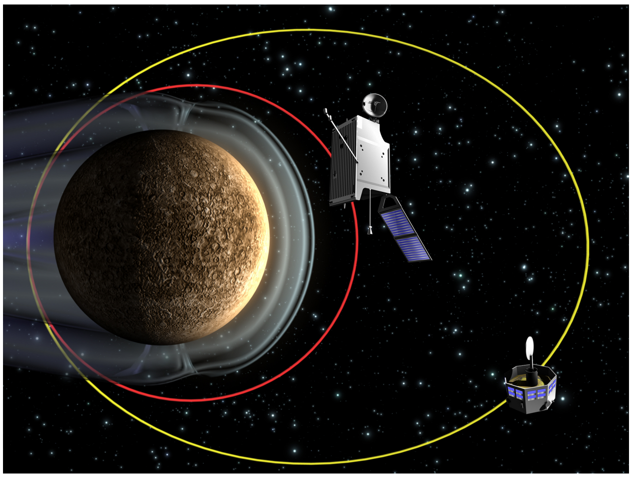

Figure 1.3: BepiColombo MPO and MMO orbits representation

proximity to the planet's surface means a larger thermal flux due to the planet infrared emission and albedo, added to the Sun's flux. MESSENGER's orbit has the periherm at 60° northern latitude and is highly eccentric (see section 1.2.2), therefore only a small fraction (less than 5%) of the orbit is spent at low altitude in the hottest thermal environment. As a consequence, the high resolution coverage is concentrated in the northern hemisphere. BepiColombo MPO's orbit is polar, with low eccentricity (400 x 1508 km of altitude), and with a period of 2.3 h, and the full high-resolution coverage is one of the main scientific objectives.

Anyway, with MESSENGER and BepiColombo, a mutually beneficial synergy is foreseen: the first can be used as a pathfinder for BepiColombo. In particular, MESSENGER observations can target high-resolution measurements for BepiColombo. Additional observations and the better downlink capabilities will allow BepiColombo to extend altimetric coverage and radio occultation observations while also extending the temporal baseline for gravitational physics measurements. Finally, the cooperative use of ground stations will provide opportunities for downlinking data that would not otherwise be present. Opportunities for cooperation in the magnetosphere include a baseline of observations of how Mercury's magnetosphere evolves over a solar cycle, something made possible by the different arrival times of the spacecraft. Mercury magnetospheric coverage by MESSENGER focuses on polar measurements while MMO coverage, coordinated with the other BepiColombo element, explicitly targets Mercury's magnetospheric structure and variations.

The selection of MESSENGER and BepiColombo offers a unique opportunity. Even though the two missions are not formally joined programmatically, each brings unique capabilities to a long overdue, detailed exploration of Mercury planet. By pursuing international cooperation, both teams have established lines of communication that will ensure that the maximum amount of new knowledge will be returned to the international scientific community and that the total knowledge returned will be grater than the sum of the two parts (McNutt et al., 2004).

2

BEPICOLOMBO RADIO SCIENCE EXPERIMENT

2.1 THE MORE EXPERIMENT

Precise orbit determination of deep space probes is not only needed for the navigation of the spacecraft itself. Thanks to the nowadays attainable high accuracy, fundamental dynamical model parameters can be estimated in the process with excellent precision. Most of the current knowledge on the planetary gravity fields and interiors has been derived by spacecraft tracking. Interplanetary tracking systems rely on microwave links for obtaining the key navigational data, namely the frequency shift and the propagation time of radio signals. These observable quantities are input to complex orbit determination codes, where the observed quantities are compared with their predicted values to produce, by means of residuals minimization, an estimate of the spacecraft state and other parameters of the model.

The radio science experiments of the mission BepiColombo (MORE, Mercury Orbiter Radio science Experiment) have been designed to give unequivocal answers to the main problems about Mercury's deep internal structure and to fully exploit the unique location of the planet in the Solar System for testing theories of gravity. BepiColombo's radio science experiments will provide (Iess et al., 2009; MORE Team, 2011):

- the harmonic coefficients of the gravity field through degree and order 25, with an accuracy up to 10^{-9}, depending on the degree and order (degree 2 with Signal to Noise Ratio SNR $\approx 10^4$; degree 10 with SNR ≈ 300 and degree 20 with SNR ≈ 10),

- the time-varying part of the gravitational potential due to solar tide (the Love number k_2), with a relative accuracy of 1-2%

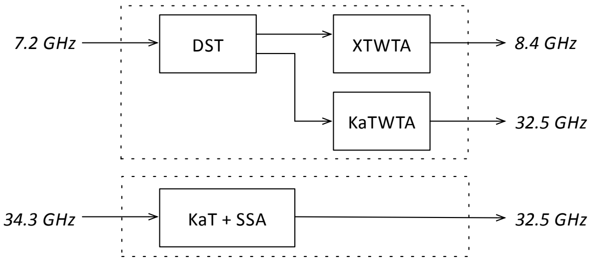

Figure 2.1: KaT and DST units

- the moments of inertia of the whole planet and its mantle, computed from the amplitude of the physical librations in longitude and the obliquity (obtained from optical imaging of the surface and radio observations),
- the post-Newtonian parameters of metric theories of gravity (especially β, γ and η),
- the gravitational oblateness of the Sun J_2,
- upper limits to the temporal variation of the gravitational constant G.

The key instrument is a Ka-band transponder (KaT) onboard the MPO (Iess and Boscagli, 2001), enabling a high phase coherence between uplink and downlink carriers and supporting a wideband ranging tone, but MORE is a system-level experiment, since not only data from KaT will be used: ancillary information on the spacecraft, scientific data of other onboard instruments and on ground data will be exploited as well. The other crucial onboard elements of the MORE experiments, besides the KaT, are the TT&C Deep Space Transponder (DST), the high gain antenna (HGA) and the accelerometer (ISA, Italian Spring Accelerometer). On ground, a deep space antenna, with Ka-band uplink capability is necessary, and the baseline foresees the use of DSS 25 (located in Goldstone, CA), while the ESA Cebreros antenna is expected to provide the X/X and X/Ka links, for telecommand, telemetry and communication. In addition, the final global fit and orbit reconstruction can incorporate also laser-altimetric and optical observables provided by the onboard laser altimeter (BELA, BEpicolombo Laser Altimeter) and high-resolution camera (SIMBIO-SYS, Spectrometers and Imagers for MPO BepiColombo Integrated Observatory System).

Kat and DST are two completely separated units (see figure 2.1) and enable a two-way, multi-frequency radio link in X/X (7.2 GHz uplink / 8.4 GHz downlink), X/Ka (7.2 / 32.5 GHz) and Ka/Ka band (34 / 32.5 GHz) providing range rate accuracies of 3 μm/s at 1000 s integration times, nearly independent from solar elongation angle (Iess et al., 2009). This configuration, already implemented for the Cassini mission (Bertotti et al., 2003b; Tortora et al., 2004), allows a complete cancellation of plasma noise, the dominant noise source in S and X band radio links (Bertotti et al., 1993). A novel wideband ranging system (WBRS), based upon a pseudo-noise modulation scheme at 24 Mcps, will provide range observables accurate to 20 cm (two-way) (Iess and Boscagli, 2001).

The effects of non-gravitational accelerations on the spacecraft dynamics (quite large in the harsh hermean environment) will be removed to a large extent thanks to the ISA accelerometer (Iafolla and Nozzoli, 2001). These instrument readouts will be sent to ground in the telemetry stream and referenced to the phase center of the high gain antenna. The orbit determination code will then use a smoothed version of the accelerometer measurements to integrate the equation of motion, effectively realizing a software version of a drag-free system.

MORE is, therefore, a complex of measurements and scientific goals; we can distinguish three different experiments, but it is not possible to separate them neatly in independent studies, since each of them depends to some extent upon the intermediate and final results of the others: the gravimetry experiment, with the goal of determining the gravity field of Mercury, a rotation experiment, for estimating the rotation state of Mercury and a relativity experiment, to determine the post-Newtonian parameters and other quantities of interest in the very accurate dynamic modeling of the Solar System, such as the mass and the dynamic oblateness of the Sun.

Such a complex experimental setup will also allow a highly precise reconstruction of the MPO orbit around Mercury (of the order of 0.1 - 1 m in the radial direction). The position of the spacecraft in the hermean frame (whose origin is defined by zeroing the dipole terms in the harmonic expansion of the gravitational potential) will be used for the appropriate referencing of the laser altimetric measurements and the images from the high-resolution camera. The combination of altimetric and gravity measurements will provide the topographic heights, a crucial information to determine the structure of Mercury's crust and outer mantle.

The along- and cross-track position of the spacecraft are crucial for the rotation experiment, aiming to determine the rotational state of the planet by means of optical tracking of surface landmark. The pole position and physical librations in longitude will be obtained from a precise georeferencing of high-resolution images (5 m pixel size at pericenter). The final accuracy of this experiment rests not only upon an accurate knowledge of the spacecraft position, but also on the quality of the attitude reconstruction. The onboard star trackers and gyroscopes should allow an accuracy of 1 - 2 arcsec. In addition, the spacecraft design ensures a high stability of the optical alignment between the star trackers and the camera.

A full numerical simulation of the Radio Science Experiment was carried out in the early phases of the BepiColombo project to verify the attainable accuracies in the gravity field determination and their compatibility with the scientific objectives of the mission. The results of the full cycle data simulation confirmed that the BepiColombo Radio Science Experiments can achieve the stated science goals, and in some cases even exceed the specifications (Milani et al., 2001). Later, a new set of numerical simulations has been carried out, taking into account the development in the spacecraft design, the mission profile and the tracking system (Genova et al., 2012; Marabucci et al., 2010).

2.1.1 *Instrument and observables*

The target accuracy for range and range rate observables is hindered by plasma contributions (interstellar gas, solar corona, solar wind, Earth ionosphere), orbit dynamics, Earth troposphere variations, thermal noise and Allan Deviation due to oscillator frequency instabilities (Asmar et al., 2005). The Radio Frenquecy Subsystem (RFS) is the base of the multi-frequency link architecture, mandatory for plasma contribution cancellation.

The on-board Radio Frequency System is composed by the following units (Simone et al., 2008):

- two X/X/Ka DST units operating in hot redundancy for the receiving section and cold redundancy for the transmitting one. They implement together with the telecommand and telemetry also the carrier frequency and ranging turn-around functions needed for spacecraft navigation and radio science experiment,
- two 35W X-Band TWTAs (Travelling Wave Tube Amplifier), main and redundant, that provide the necessary RF amplification to the X band signal coming from the DST units,
- two 35W Ka-Band TWTAs, main and redundant, to amplify the Ka band RF signal coming from the DST units,

- one Dual Band High Gain Antenna (HGA), used to perform both radio science experiment and spacecraft communications in both X and Ka bands,
- one X-Band Medium Gain Antenna (MGA), not used for RSE,
- two X-Band Low Gain Antennas (LGAs), not used for RSE.

Measurements of the Doppler shift at ground station is a key point in estimating the relative radial velocity between the spacecraft and the ground station. The range rate of a probe over a given interval is measured by monitoring the unwrapped carrier phase change that results from the spacecraft motion. For ranging measurements, the primary observable is the delay of the received signal with respect to the transmitted ranging signal. In general, the ranging signal is composed of a ranging clock modulated by a code for ambiguity resolution. The clock delay measurement, along with the code ambiguity resolution, indicates the absolute range at a given time.

For radio science experiment performance, one of the main error sources for accurate Doppler and range measurements comes from plasma scintillation (solar, interplanetary, and ionosphere contributions). Indeed, the medium causes an additional time varying contribution in the ranging delay and a shift of the carrier frequency in Doppler measurements. In order to cope with these effects the BepiColombo mission uses a multi-frequency radio link in the X/X and X/Ka bands via the X/X/Ka Deep Space Transponder (DST) and in the Ka/Ka band via the KaT unit. The approach is the same used for the Cassini mission, but in this case the multifrequency link is implemented also for the ranging function.

As reported in Asmar et al. (2005), the so-called plasma-free (non dispersive) sky frequency is obtained as a linear combination of the three X/X, X/Ka and Ka/Ka links. The accuracy in the Ka/Ka link results to be much more important in the computation for determining the desired synthetic nondispersive observables, than the other two links. Therefore the radio science experiment success relies significantly on the KaT unit performance.

The KaT design for the BepiColombo radio science experiment is based on a combination of advanced signal processing algorithms and modern technological implementation. The KaT core, based on a digital architecture, leads to the following advantages with respect to a fully analog solution:

- optimization of carrier acquisition and tracking performance,
- inclusion of PN ranging processing capabilities (demodulation and re-modulation),

- design flexibility with receiver tuning based on programmable constants,
- all-digital modulation capabilities based on Direct Digital frequency Synthesis.

2.2 SIMULATION SETUP

Numerical simulations of the gravity experiment has been carried out in the past and are the basis for the present work. In this chapter, we report on the final setup, developed to take into account changes in spacecraft design, mission operations, and tracking system.

The initial MPO orbit around Mercury is polar with pericenter and apocenter altitudes respectively at 400 km and 1500 km. The nominal mission duration is one (terrestrial) year and support from ground is foreseen from Cebreros, for TT&C, and from DSS25 (Goldstone), specifically for the radio science experiment. The daily tracking period from each station is approximately 8 hours, but loss of the radio link due to occultations has also been accounted for.

The spacecraft design, driven by the need of reducing the mass, required the use of relatively low capacity momentum wheels and entailed momentum dumping maneuvers approximately every 12 hours, instead of every 24 hours, as initially foreseen. During these maneuvers, the unbalanced thrusters will produce a large along-track ΔV, therefore degrading the a priori knowledge of the spacecraft state and affecting the accuracy in the estimation of the gravity field. Although the knowledge of the ΔV associated to desaturation maneuvers is possible to a level of 2 - 5% (1.2 - 3 mm/s), the residual, unmodeled ΔV is still sufficiently large to cause substantial errors in the state propagation. In general, desaturation maneuvers will be controlled by onboard software and will take place outside the tracking period dedicated to the radio science experiment, while it is foreseen to have one maneuver inside the X-band tracking period (see figure 2.2), to allow distinguishing the effects of the two burns. In order to consider, in our simulations, the error in the knowledge of the ΔV, the model used to generate the simulated observables and the estimation model differ in the magnitude of the impulsive burns of the desaturation maneuvers of a quantity equal to this lack of the knowledge, and an appropriate apriori uncertainty is associate to this value.

Mercury's gravity field is expanded in spherical harmonics up to degree 30. The coefficients up to degree 20 are equal to the HgM002 values, the estimated gravity field model by MESSENGER team (Smith

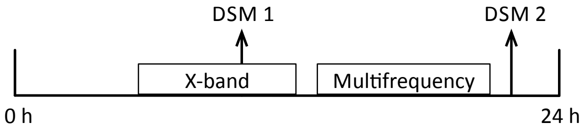

Figure 2.2: 24 hours arc configuration

et al., 2012). The remaining higher degrees are simulated following the Kaula's rule. Being

$$C_l^2 = \frac{1}{2l+1} \sum (C_{lm}^2 + S_{lm}^2) \tag{2.1}$$

this empirical law describes the decreasing of the order of magnitude of the coefficients with the degree l, according to:

$$C_l^2 = A_k \frac{10^{-10}}{l^4}, \tag{2.2}$$

where the constant A_k is assumed equal to 9 for Mercury (Milani et al., 2001). Tidal effects have been considered, with a dynamic Love number k_2 set to 0.3 (Bertotti et al., 2003a).

The high sensitivity accelerometer (ISA, or Italian Spring Accelerometer) is hosted onboard the MPO with the goal of measuring the non-gravitational accelerations acting on the spacecraft. The non-gravitational accelerations (direct solar radiation and thermal emission from the planet) must be limited or compensated to a level of 10^{-9} g/$\sqrt{\text{Hz}}$, in order to meet the requirements imposed by the radio science experiment. Solar radiation alone causes (at 1000 s integration times) an effect which is three order of magnitude larger than the above value, because of the vicinity of Mercury to the Sun and the large temperature of the planet surface. ISA has the essential task of providing the information needed to transform the real spacecraft into a virtually drag-free test particle during the orbit determination process. Assuming that the accelerometer ISA will be operational as specified, non-gravitational effects, such as solar radiation pressure or planetary thermal radiation, have not been taken into account. Accelerometer noise, of the order of 10^{-6} cm/s^2 is added, in the form of periodical accelerations, with orbital period, as reported in Milani et al. (2001).

Simulated range rate observables are the input to the estimation process. The error budget of MORE states an Allan deviation of 1.6 10^{-14} at 1000 s integration time for Ka band, two ways (MORE Team, 2011). Starting from such values of the Allan deviation, a white Gaussian noise of 1.3 mHz has been added to the simulated data at 10 seconds for an equivalent X band.

2.3 ORBIT DETERMINATION

The problem of determining the best estimate of the position and velocity of a spacecraft, whose initial state is unknown, with a dynamical model containing other unknown parameters, from observations influenced by random and systematic errors, using a mathematical model that is not exact, is referred to the orbit determination problem.

2.3.1 *Classical batch filter*

Deep space probes are visible from Earth stations for several hours per day, but in general are supported by only one ground station. In a classical approach, all collected data are processed through a batch filter, in order to improve the knowledge of the state vector and of free parameters.

In the general orbit determination problem, both the dynamics and the measurements involve arbitrary nonlinear relationships. We can write the dynamics and observations equations as:

$$\dot{\mathbf{X}} = F(\mathbf{X}, t) \qquad \mathbf{X}(t_k) \equiv \mathbf{X}_k, \tag{2.3}$$

$$\mathbf{Y}_i = G(\mathbf{X}_i, t_i) + \boldsymbol{\epsilon}_i \qquad i = 1, \ldots, l, \tag{2.4}$$

where $\mathbf{X}_k$ is the unknown n-dimensional vector of solved-for parameters (spacecraft position and velocity components and free parameters of the dynamical model) at the time t_k, and $\mathbf{Y}_i$ for $i = 1, \ldots, l$, is a p-dimensional set of observations with an error $\boldsymbol{\epsilon}_i$, that is used to obtain the best estimate of the unknown vector $\mathbf{X}_k$, according to an optimum criterion. In general, $p < n$ and $m = p \times l \gg n$.

These equations can be linearized in terms of state deviation and observation deviation vectors, with respect to a reference solution, indicated with $()^*$:

$$\mathbf{x}(t) = \mathbf{X}(t) - \mathbf{X}^*(t), \tag{2.5}$$

$$\mathbf{y}(t) = \mathbf{Y}(t) - \mathbf{Y}^*(t). \tag{2.6}$$

Therefore, the linearized problem can be written as:

$$\dot{\mathbf{x}}(t) = \mathbf{A}(t)\mathbf{x}(t), \tag{2.7}$$

$$\mathbf{y}_i = \tilde{\mathbf{H}}_i \mathbf{x}_i + \boldsymbol{\epsilon}_i, \tag{2.8}$$

where:

$$\mathbf{A}(t) = \left[\frac{\partial F(t)}{\partial \mathbf{X}(t)}\right]^*, \tag{2.9}$$

$$\tilde{\mathbf{H}}_i = \left[\frac{\partial G}{\partial \mathbf{X}}\right]_i^*. \tag{2.10}$$

Thanks to the transition matrix $\boldsymbol{\Phi}(t_i, t_k)$, all the observables in the batch can be referred to the initial state:

$$y_i = \mathbf{H}_i \mathbf{x}_k + \epsilon_i, \tag{2.11}$$

where

$$\mathbf{H}_i = \tilde{\mathbf{H}}_i \boldsymbol{\Phi}(t_i, t_k). \tag{2.12}$$

Therefore one can write:

$$\mathbf{y} = \mathbf{H}\mathbf{x} + \boldsymbol{\epsilon}, \tag{2.13}$$

where $\mathbf{y}$ is a m-dimensional vector of observables, $\mathbf{x}$ is the n-dimension vector of unknown parameters, $\mathbf{H}$ is the $m \times n$ mapping matrix, and $\boldsymbol{\epsilon}$ is the observation errors vector.

It is also possible to associate a weighting factor to each observable, and therefore the diagonal weighting matrix $\mathbf{W}$ is considered. The weighted last square solution selects the estimate of $\mathbf{x}$ as that value that minimizes the weighted sum of the square of the calculated observation errors. The performance index is:

$$J(\mathbf{x}_k) = \frac{1}{2}\boldsymbol{\epsilon}^T \mathbf{W} \boldsymbol{\epsilon}. \tag{2.14}$$

By minimizing the cost function 2.14, the solution is:

$$\hat{\mathbf{x}}_k = (\mathbf{H}^T \mathbf{W} \mathbf{H} + \bar{\mathbf{W}}_k)^{-1} (\mathbf{H}^T \mathbf{W} \mathbf{y} + \bar{\mathbf{W}}_k \bar{\mathbf{x}}_k), \tag{2.15}$$

where $\bar{\mathbf{x}}_k$ and $\bar{\mathbf{W}}_k$ represent respectively the a priori estimate and covariance matrix of $\mathbf{x}_k$. The iteration of this process allows obtaining the best estimate of $\mathbf{x}$ in the case of planetary flybys or trajectories of a few days.

The limit of this formulation is represented by the difficulty of inverting the information matrix $\mathbf{\Lambda} = (\mathbf{H}^T\mathbf{W}\mathbf{H} + \bar{\mathbf{W}}_k)$, which is often ill-conditioned. This obstacle can be overcome by the square-root formulation. The square root of the information matrix is $\mathbf{\Lambda}^{\frac{1}{2}}$, such that:

$$\mathbf{\Lambda} = \mathbf{\Lambda}^{\frac{T}{2}}\mathbf{\Lambda}^{\frac{1}{2}}. \tag{2.16}$$

In the considered case, the square root of the information matrix is constructed as:

$$\mathbf{\Lambda}^{\frac{1}{2}} = \left(\begin{array}{c} \mathbf{W}^{\frac{1}{2}}\mathbf{H} \\ \hline \bar{\mathbf{W}}_k \end{array}\right). \tag{2.17}$$

This matrix can be decomposed into a product of an orthogonal matrix Q and a triangular matrix R, by means of a QR factorization:

$$\mathbf{\Lambda}^{\frac{1}{2}} = QR. \tag{2.18}$$

Therefore, it results:

$$\mathbf{\Lambda} = \mathbf{\Lambda}^{\frac{T}{2}}\mathbf{\Lambda}^{\frac{1}{2}} = \mathbf{R}^T\mathbf{Q}^T\mathbf{Q}\mathbf{R} = \mathbf{R}^T\mathbf{R}. \tag{2.19}$$

The inverse of the information matrix can be computed as:

$$\mathbf{\Lambda}^{-1} = \mathbf{R}^{-1}\mathbf{R}^{-T}. \tag{2.20}$$

In this way, the condition number of the matrix to invert has a condition number that is the square root of the condition number of the information matrix $\mathbf{\Lambda}$.

Nevertheless, this solution may not be sufficient when the dynamics of the spacecraft is quite complicated and when there is a large number of solve-for parameters in $\mathbf{x}$. In such cases, the trajectory could be subdivided into shorter arcs (i.e. single day). It allows obtaining convergence by using the multi-arc approach, that improves considerably the estimation of the global parameters.

2.3.2 *Multiarc approach*

In several space geodesy experiments the number of parameters to be determined is quite large. This problem is, in many cases, severe to the point that a single batch estimation becomes impractical. In addition, deterministic models are unable to reliably account for non-gravitational perturbations. In many cases a multi-arc method alleviates these problems, although the presence of disturbances may end up in a divergence in the estimation process.

In a multi-arc approach the orbit of the spacecraft is fragmented into different arcs, corresponding to non-overlapping time intervals. Each arc has its own initial conditions and it is completely independent from the others, because the initial conditions of the state vector of the space vehicle do not depend in any way on the orbital propagation of the preceding arcs.

The estimated parameters are divided into two categories: the *local parameters*, pertaining to the single arc (i.e. state vector, maneuvers and periodic acceleration), and *global parameters*, independent of time and pertaining to all arcs (the mass and the gravitational harmonics of the central body, for example).

In this way, the total number of parameters increase, since each arc has its individual set of local parameters. The main goal of this over-parameterization is to absorb the effects and errors caused by unmodelled dynamics, errors that accumulate with time. Therefore, the length of every arc should be chosen so as to maintain the errors in the dynamical model at a level compatible with the observation errors. The arc length must be chosen judiciously: if too long, the errors accumulate, if too short the solution becomes unstable. For instance, arcs characterized by favourable geometrical conditions are to be privileged, whereas those during which the spacecraft performs manoeuvres are to be disregarded.

In the multiarc approach, the solve-for parameters vector is, therefore, splitted into two parts:

$$\mathbf{x} = \begin{pmatrix} \mathbf{g} \\ \mathbf{l} \end{pmatrix}, \tag{2.21}$$

distinguishing global and local parameters respectively. The vector $\mathbf{l}$ is further divided into vectors $\mathbf{l}_i$, one for each arc, and following the definition of local parameters, the partial derivatives of observations $\mathbf{z}_i$ occurred in the i-th arc, with respect to local parameters of a different arc (l_j with $j \neq i$) will be null. Supposing to have three arcs, the mapping matrix would have the following structure:

$$\mathbf{H} = \begin{pmatrix} \frac{\partial \mathbf{z}_1}{\partial \mathbf{l}_1} & 0 & 0 & \frac{\partial \mathbf{z}_1}{\partial \mathbf{g}} \\ 0 & \frac{\partial \mathbf{z}_2}{\partial \mathbf{l}_2} & 0 & \frac{\partial \mathbf{z}_2}{\partial \mathbf{g}} \\ 0 & 0 & \frac{\partial \mathbf{z}_3}{\partial \mathbf{l}_3} & \frac{\partial \mathbf{z}_3}{\partial \mathbf{g}} \end{pmatrix} \tag{2.22}$$

and the solution of the orbit determination problem can be computed again as in equation 2.15, also applying the QR factorization to the square root of the information matrix.

Anyway, the multi-arc approach could manifest some difficulties in convergence when in the single arcs the number of parameters to be estimated is too large, as in the case of the MORE experiment with the MPO. In these cases, a sequential update of the dynamical model improves the estimation process.

2.3.3 *Batch sequential filter*

The accumulation of the errors due to unmodelled effects and the instability of the solution caused by the large number of solve-for parameters in each arc could lead to a divergence in the trajectory reconstruction, making the multiarc method ineffective. Numerical simulation of the BepiColombo Radio Science experiment proved that the multiarc approach is not sufficient to correctly retrieve MPO's orbit. Therefore, a batch-sequential filter has been developed in order to cope with these issues.

With the batch-sequential method, the dynamical model is updated and improved every time that additional, not too long data batches are included in the solution (see step I in figure 2.3). The sequential processing of short batches improves the estimation of the state vector, batch after batch. The choice of the batch length is particularly important for a fast convergence and a good accuracy of the final orbital solutions and it is a trade off between the estimation accuracy of the global and local parameters.

A single batch is processed following three essential steps:

- single arc estimation of a limited number of arcs (N);
- multi-arc estimation with initial conditions and a priori uncertainties equal respectively to the estimated values (weighted

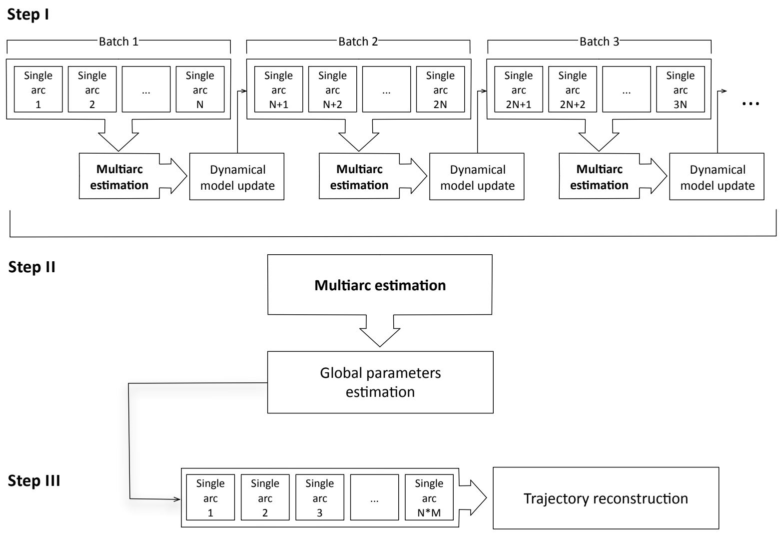

Figure 2.3: Sequential batch estimation (M batches of N arcs each)

mean for the global parameters, with formal uncertainties as weights) and a priori uncertainties of the single arc estimation;

- update of the dynamical model parameters of the consecutive batch, with the global parameters estimated in the multiarc.

With this procedure, the processing of the arcs in the following batch benefits from an improved dynamical model, thus allowing a better reconstruction of the trajectory. In addition, this sequential updating leads also to improved estimates of the global parameters, which reach convergence after a limited number of batches.

However, both the state vector and the global parameters estimation may be still improved. Indeed, these batches processing is only the first part of a three-step process. The first step, already illustrated, is important to prepare the initial conditions of each single arc and improve the knowledge of the dynamical model batch after batch. The second step (see step II in figure 2.3) uses the improved dynamical model to initialize a complete global multi-arc estimation. The output of this step is considered as our best estimate of global parameters. Finally (see step III in figure 2.3), using the recovered dynamical model, the trajectory can be estimated with the required accuracy in the third step, by means of a final single arc estimation.

3

CROSSOVERS IN ORBIT DETERMINATION

3.1 MOTIVATIONS AND OBJECTIVES

In this chapter, we focus on the motivations of this work, its objectives and what has been done to reach them. The basic idea is to integrate the laser altimeter measurements in the orbit determination process, and the objective is to evaluate advantages and disadvantages of using these observables for the BepiColombo mission.

Two of the main scientific goals of the mission are the determination of Mercury's gravity field and topography. With this work, we want to assess the best strategy to recover them, choosing between a global fit with radio and laser observables, or a two step approach, in which the radio data are used to estimate the gravity field of the planet and to reconstruct the spacecraft trajectory, and then this is used to determine the topography.

Crossover observables, computed as difference between two laser altimeter measurements in a point where two ground tracks intersect, produce a constrain for the spacecraft trajectory. In fact, if the spacecraft position was exactly known and the detection of the crossover was extremely precise, the difference between the two laser altimeter measurements would be equal to the difference between the radial positions of the spacecraft at the times of the intersection. In reality, the orbit is not exactly known, and there will be errors in the crossover location and in the laser altimeter measurements, so the two differences will not be equal, but the residuals can be minimized in an iterative process by correcting the spacecraft position, and consequently the crossover location. The information contained in the crossover observables affects directly only the determination of the radial component of spacecraft position. However, the cross track and the along track components are indirectly affected through the dynamics. Therefore, it is necessary to recompute latitudes and longitudes of the crossovers as the orbit solution is iterated.

Global analysis of crossover residuals can be used to mitigate the error in the radial positioning of the spacecraft and can contribute to the determination of interesting geophysical parameters. Crossovers were used for oceanographic and geophysical applications, to evaluate the accuracy of SEASAT ephemerides and altimetry timetag and in gravity anomalies recovery (Shum et al., 1990).

Altimetry, in the form of crossovers, has been used to improve the orbit and the attitude knowledge of Mars Global Survey (MGS). In Rowlands et al. (1999), the MGS Science Phasing Orbit-1, from late March through April 1998, is analyzed and it is demonstrated that the addition of crossover constraint equations improves the orbit solution obtained previously using only radio observables. The crossover minimization process directly affects all components of the orbit, thanks to the increased sensitivity to along- and cross-track orbit error of the laser altimeter over sloping terrains. In this formulation, crossover location can be corrected in order to minimize the height discrepancy.

Besides, the estimation of spherical harmonic coefficients up to degree 60 of the Mars gravity field has been carried out using X-band tracking data of MGS (data noise of 0.1 mm/s over a 10 s counting interval), from October 1997 to February 2000 and crossover observables between March and December 1999 (GMM-2B, Goddard Mars Model 2B). A comparison with a solution obtained without altimetry data reveals that the crossover observables enhanced the sensitivity to the low-degree odd zonal harmonics and to the high-degree zonals above degree 50. The orbit tests provide some evidence that the addition of the MOLA altimeter crossovers strengthens the gravity solution, since the total orbit discrepancy in trajectory overlap is reduced from 12.3 to 5.7 m (Lemoine et al., 2001).

Crossovers have been used also for Lunar Reconnaissance Orbiter (LRO). The accuracy of the S-band radio tracking system (1 mm/s for the White Sand station and 1.5 - 3 mm/s for the USN stations) were too large to enable the position reconstruction with the desired precision. The inclusion of altimetric data from the onboard Lunar Orbiter Laser Altimeter (LOLA) strongly improved the accuracy of the spacecraft trajectory reconstruction: the overall overlap RMS (Root Mean Square) values decreased by about 70% (from 70 m to 23 m in total position) (Mazarico et al., 2011).

BepiColombo will carry onboard a novel tracking system, as reported in section 2.1 and a laser altimeter, BepiColombo Laser Altimeter (BELA, see section 3.2). We carried out numerical simulations in order to evaluate the contribution of crossover observables in the orbit determination process. The extremely good accuracy of the multifrequency link (1 μm/s at 1000 s) allows to reconstruct the trajectory with excellent precision and we expect crossover observables cannot improve the solution. It is in line with the results of LRO and MGS: when the accuracy of radio data increases (from S- to X- and then to Ka-band), the crossovers impact decreases. However, from the BepiColombo radio science experiment's point of view, this result has a direct consequence for the spacecraft trajectory and planet topography reconstruction. Indeed it means that the trajectory can be estimated using only radio observables with the best achievable accuracy, and the topography can be retrieved trusting in this trajectory. Furthermore, being mission independent, what has been done for this thesis can be used in the future for other missions with radio science and laser altimeter experiments.

All the numerical simulations reported in this work were carried out with the JPL's software ODP (Orbit Determination Program (Panagiotacoupulos et al., 1974)). This software has been developed over a period of 40 years and it has enabled accurate navigation of a large number of NASA's planetary exploration missions. The software is formed by a number of subprograms with different aims: to set the dynamical model, to propagate the trajectory of the desired bodies, to compute visibility from ground stations, to generate computed observables, and, finally to estimate the required parameters, computing residuals and partial derivatives.

The core of the orbit determination process is the estimation filter. This subprocess compares the observed data to the predicted ones, computed by using the initial estimated spacecraft trajectory, and makes subsequent adjustments to the solve-for parameters, so that the predicted data compare more closely with the real observations.

In our laboratory, a new least square filter code has been developed and tested, in order to include new parameters and/or new observables in our estimations. Thanks to this code, it was possible to include the crossover observables in the orbit determination process, providing residuals and partial derivatives with respect to the parameters we want to estimate (see section 3.3.3 and 3.3.4).

Previous numerical simulations, with only radio observables, constitute the basis of this work and are the terms for comparison to point out the contribution of crossover observables. After having assessed the setup and the estimation process, it has been possible to complicate the structure, by including crossover.

A dedicated collaboration with the BELA team has been necessary, in order to improve our knowledge of the laser altimeter instruments, and its measurements and expected noise, to examine in depth the crossovers detection problem and to compare and discuss results.

3.2 BELA

The BepiColombo Laser Altimeter (BELA) is one of the instrument onboard the MPO and it is part of a larger geodesy and geophysics package, together with radio science and high resolution imaging (Thomas et al., 2007; Gunderson et al., 2006). The measurement concept is simple: the time of flight of a pulse, Δt, from the onboard laser to the planet's surface and back is measured and it's translated into distance z by the expression

$$z = \frac{c\Delta t}{2}, \tag{3.1}$$

where c is the speed of light. Additional measurable parameters extracted from the return pulse provide information about sub-footprint surface structures and surface albedo.

The scientific objectives of the experiment are to measure:

- Mercury's figure (mean radius, polar radius and equatorial radius), to establish accurate reference surface,
- the topography variations relative to the reference figure and a geodetic network, based on accurately measured position of topographic features,
- the tidal deformation of the surface
- the surface roughness, local slopes and albedo variations.

The instrument has been studied considering the orbit of the MPO and the harsh environment of Mercury. The orbit will precess from a periapsis of 20°S latitude to 20°N latitude, during the nominal duration, hence, to guarantee coverage from pole to pole, BELA needs to acquire data up to 1055 km of altitude.

The figure of merit used to evaluate the performance of a laser altimeter is the probability of false alarm (PFA): it is the probability that the system fails in detecting the return pulse. The range resolution of the instrument depends on the laser pulse width and the timing precision of the electronics. Besides, an independent knowledge of the platform pointing angle and motion is needed for determining the surface topography. Variations in laser pointing angle become bias and spacecraft vertical motion can be confused with topographic variability. Therefore, high resolution laser altimetry requires pointing control to maintain nadir pointing and accurate knowledge of spacecraft attitude. An expression for time of flight uncertainty has been derived in Gardner (1992), taking into account surface roughness, beam curvature, viewing angle, surface slope, spacecraft attitude measurement errors, and system effects.

BELA will be a 10 Hz system, with a pulse width of 5.5 ns (full width, half maximum) and a beam divergence of 50 µrad (full angle), with a mass of 14 kg and a power consumption of 43.2 W. The estimated ranging accuracy from the experiment under nominal conditions is 1 m and under optimum conditions 0.25 m although errors in the knowledge of the spacecraft pointing are expected to dominate the final error budget.

3.3 METHOD

In this section, we want to summarize what has been done in order to include crossover observables in the orbit determination process, and to carry out simulations of the MORE gravity experiment with both radio and crossover observables. First, it was necessary to simulate laser altimeter observables, adding a realistic noise on the measurements, to detect the crossover location (times, colatitude and longitude), to compute the partial derivatives of crossover observables with respect to the solve-for parameters and, finally, to integrate them in the mapping matrix of the least square filter. In the following paragraphs, these steps are examined in depth.

3.3.1 *Simulated laser altimeter observables*

The laser altimeter measurement concept is quite simple and provides the distance between the spacecraft and the surface of the planet (see section 3.2). However, the computation of this distance is not so easy as it seems. In fact, after interaction of the laser footprint with a rough and sloping surface, the backscattered pulse may contain several nanoseconds or more of pulse spreading or distortion. Consequently, quantities as the number of photons in the return pulse, the pulse centroid time and the RMS pulse width are exploited to correctly detect the spacecraft-surface distance, and, in addition, other properties of surface, as roughness and slope (Thomas et al., 2007).

However, this goes beyond the aim of this work and will be the main task of BELA team. For our need, the simulated laser altimeter measurement $LA(t_i)$ can be reduced to a difference between the

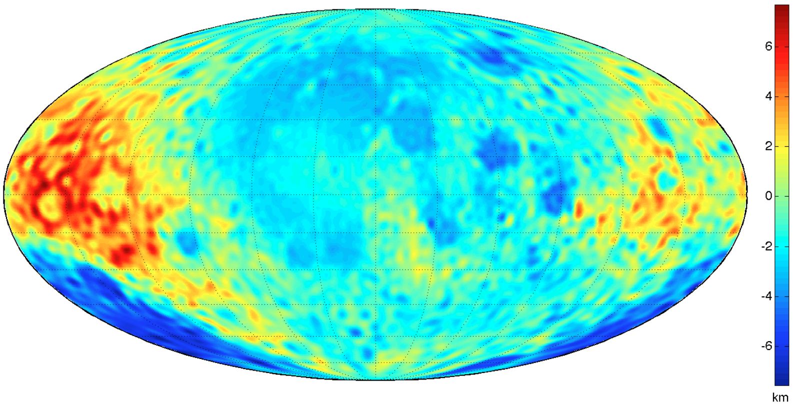

Figure 3.1: Simulated topography

radial distance of the spacecraft in a simulated trajectory $\|\vec{r}_{S/C}(t_i)\|$ and the topography of the planet in the sub-satellite point $T(\theta_i, \lambda_i)$.

$$LA(t_i) = \|\vec{r}_{S/C}(t_i)\| - T(\theta_i, \lambda_i). \tag{3.2}$$

The MPO trajectory has been propagated using a realist setup, as reported in section 2.2. Mercury topography (figure 3.1) has been simulated using a 70 degree and order spherical harmonic expansion of the topography of the Moon[1], from the mission Clementine (Goddard Lunar Topography Model 2, GLTM-2) (Smith et al., 1997):

$$T(\theta, \lambda) = \sum_{l=0}^{l_{max}} \sum_{m=0}^{l} P_l^m(\cos\theta)[C_{lm}\cos(m\lambda) + S_{lm}\sin(m\lambda)], \tag{3.3}$$

where the P_l^m are fully normalized associated Legendre functions, θ is the colatitude and λ the longitude.

In order to take into account the tidal effect of the Sun on the planet Mercury, the tidal elevation δr_{tide} is added to the simulated topography:

$$\delta r_{tide} = h_2 F_{tide}(\Psi, r) = h_2 \frac{M_{Sun}}{M_{Merc}} \frac{a^4}{R^3} \left[\frac{3}{2}\cos^2\Psi - \frac{1}{2}\right], \tag{3.4}$$

where h_2 is the tidal Love number, $\Psi(\theta, \lambda, t)$ is the angle between the line connecting Mercury's center of mass and the Sun, and the radius vector r from Mercury's center of mass to the location on Mercury's surface with colatitude θ and longitude λ at the time t, a is the mean

---

[1] `http://pds-geosciences.wustl.edu/lunar/clem1-gravity-topo-v1/cl_8xxx/topo/gltm2bsh.tab`

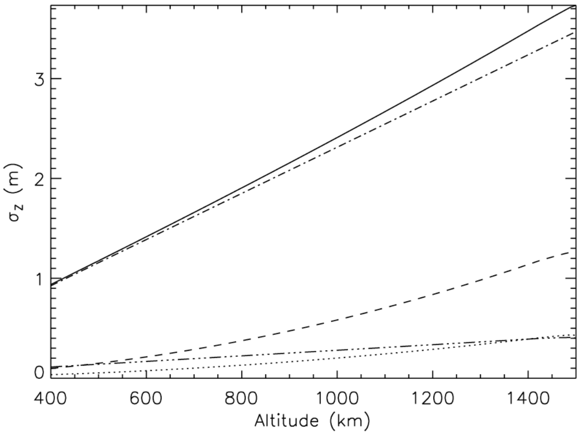

Figure 3.2: Range uncertainty according to the expression of Gardner (1992). The plotted components are uncertainties due to surface roughness (*dotted*), nadir/slope angle (*dashed*), spacecraft ponting uncertanty (*dash-dot*) and system errors (*dash-dot-dot-dot*). The *solid* line is the total uncertainty.

planetary radius, R the distance of Mercury to the Sun, and M_{Sun} and M_{Merc} are the masses of the Sun and Mercury, respectively (Koch et al., 2010).

To correctly simulate laser altimeter measurements, it is mandatory to study the expected noise of these data and to add a realistic model of this noise on the simulated observables. In Gunderson et al. (2006), a complete analysis of the BELA system has been carried out, to verify the system's performance within the challenging constraints imposed by the harsh environmental conditions around Mercury and the stringent spacecraft resource limitations. The signal to noise ratio (SNR), the false detection probabilities (PFD, see section 3.2)and the range measurements uncertainties (σ_z) are the figures of merit taken into account in this analysis.

For our purpose, only the range measurement uncertainties need to be investigated and added to the expression 3.2. A comprehensive investigation of the possible error sources for satellite laser altimeters is reported in Gardner (1992). In the figure 3.2 (actually reported in Gunderson et al. (2006), but computed using the expressions written in Gardner (1992)), all the contributions to the range uncertainty are shown: errors due to surface roughness, nadir/slope angle, spacecraft pointing uncertainty and system error. Pointing jitter results to be the dominant source of range error, especially over terrains with

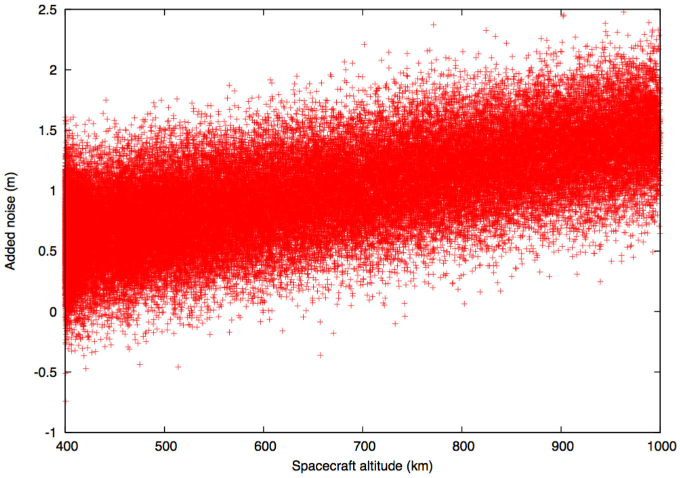

Figure 3.3: Total noise added on the simulated laser altimeter observables

large surface slope S and increases with the spacecraft altitude z. The simplified formulas used to compute this contribution $\sigma_{ponting}$ is:

$$\sigma_z \cong \sigma_{pointing} = \sqrt{2} z \tan S \, \sigma_{\Delta\Phi}, \tag{3.5}$$

where $\sigma_{\Delta\Phi}$ is the nadir pointing error.

Finally, two kinds of errors have been added to the simulated laser altimeter data: a measurement error, by means of a white Gaussian noise with RMS=30 cm, and the pointing jitter error, computed for a spacecraft altitude between 400 km and 1000 km, a Mercury's mean surface slope of 3° and 20 μrad of pointing uncertainty. The total noise added on the simulated observables is shown in figure 3.3.

3.3.2 *Crossover detection*

Once the spacecraft trajectory and the laser altimeter measurements have been simulated, we can proceed with the detection of crossovers. The problem is intuitive and seems to be easy, but it hides some computational difficulties, overall in terms of computation time.

In order to overcome this issue, the parallelization of the code is required: the ground tracks are divided into colatitude areas, and the crossover search is limited between the sections of ground tracks within a single area. The parallelization has been simply realized by means of simultaneous calls of the crossover detection code with different colatitude areas as input. The number of cores used can be set by the user.

The expected number of crossover is $n(n-1)$, where n is the number of orbits. Considering MPO polar orbit, crossovers are expected to be located close to the poles. Furthermore, we need to remind that BELA can operate up to an altitude of 1050 km, and it means that, due to the combination of this constrain and the shift of the argument of pericenter, we will have approximately the half of expected crossovers, since no laser altimeter measurements are available when the altitude of the spacecraft is too high near the poles. In the figure 3.4, the eleven ground tracks of 24 hours of the MPO trajectory are shown, with three increasing levels of zoom in, around the crossovers location.

The code has been developed in Fortran 90, using NAIF SPICE routines[2]. SPICE (Spacecraft Planet Instrument C-matrix Events) is a space geometry information system for assisting scientists in planning and interpreting scientific observations from space-based instruments, developed by NASA's Navigation and Ancillary Information Facility (NAIF).

To speed up the process and, at the same time, to maintain a good accuracy in the determination of the crossovers location, the detection process has been split into two parts. The first part is only needed to limit the portions of ground tracks where there may be a crossover. In order to isolate these parts, each tracks in the considered colatitude band is sampled. Each couple of points is linearly interpolated and intersected with the linear interpolation of each couple of points of the following track. If the computed intersection point is within the four considered points, the two ground tracks portions are stored, and will be analyzed with increased accuracy in the second part of the code. Otherwise, following couples of points are considered and the process is repeated, as long as all the couples of all the tracks are intersecting.

Due to the linearization, some intersection may be detected in points where actually the two ground tracks are not crossing. The second part of the code has the aim to reject these points and to improve the location of the real crossovers. In the interval where the crossover is supposed to be, the two involved ground tracks are sampled with higher frequency. For each longitude, the colatitude difference is computed. When the sign of these differences changes, it means that there is an intersection between the ground tracks. This part can be iterated for improving the determination of the crossover coordinates and times, by taking as extremes of the ground tracks the points immediately before and after the change of sign. Finally, times, colatitude and longitude of the crossover are determined.

---

[2] http://naif.jpl.nasa.gov/naif/

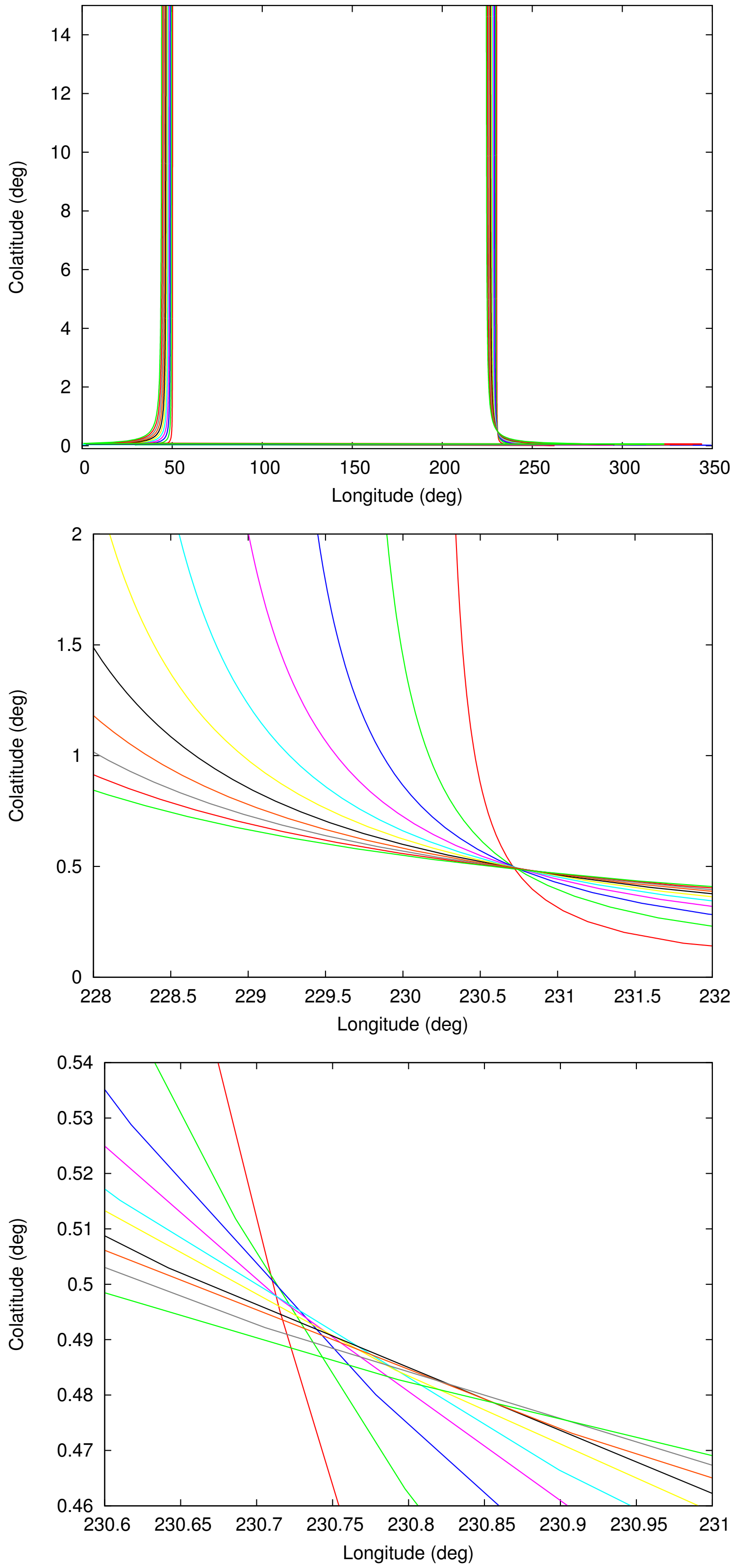

Figure 3.4: Zoom in of one-day ground tracks

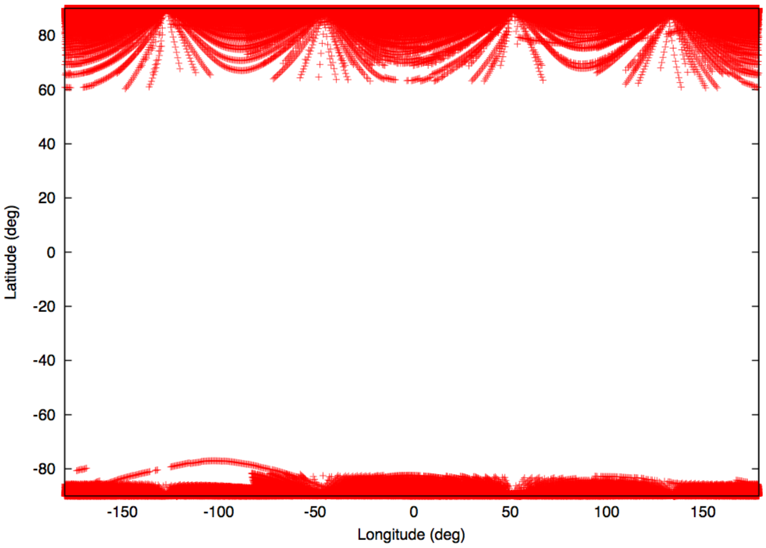

Figure 3.5: Location of crossovers in 110 days

In figure 3.5, the locations of crossovers that occurred within 110 days are shown. The number of crossovers is different between the two poles, due to BELA's operation limit of up to 1055 km. The inclination of the MPO orbit has slight variations of less than 1° around the polar configuration, caused by the perturbations acting on the spacecraft. Therefore, most of the crossovers are located at a distance of 0.2 - 0.4° in latitude from the poles. The shift of two consecutive groundtracks at the equator is less than 30 km, since the rotation period of Mercury is about 58 days and the spacecraft orbital period is 2.35 hours (see also the first image in figure 3.4). After half of the planet rotation period (and multiples), the groundtracks generate crossovers at larger distance from the poles, up to 20° from the poles.

In order to check this procedure, and to have a feeling of the precision attainable in the crossovers detection, a comparison between our software and a completely independent software, developed by the BELA team at DLR, has been carried out. Starting from the same simulated MPO trajectory, lasting 24 hours, crossovers have been detected with the two softwares and the results compared, in terms of differences in time, colatitude and longitude. Considering the period of MPO, the foreseen number of crossovers is 55, and it is correctly recovered with both softwares. Figure 3.6 shows the difference in the determination of the times of crossovers, while figure 3.7 reports the differences in colatitude and longitude of the detected crossovers. Be-

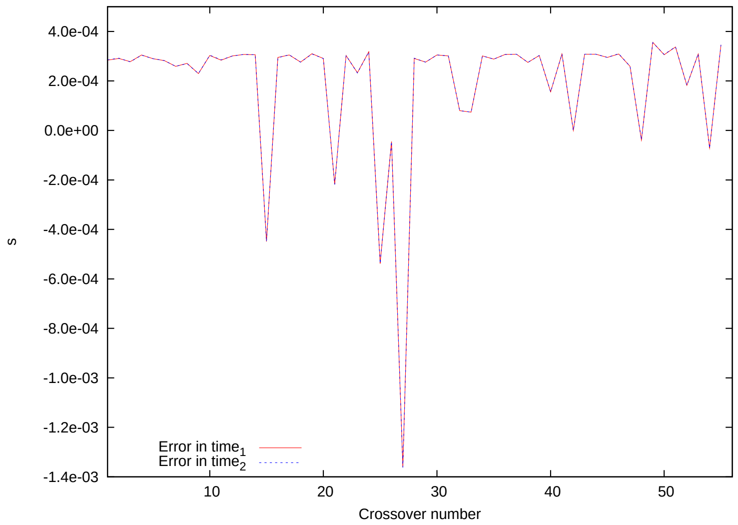

Figure 3.6: Difference in the determination of the times of crossovers t_1 and t_2, between our and DLR software

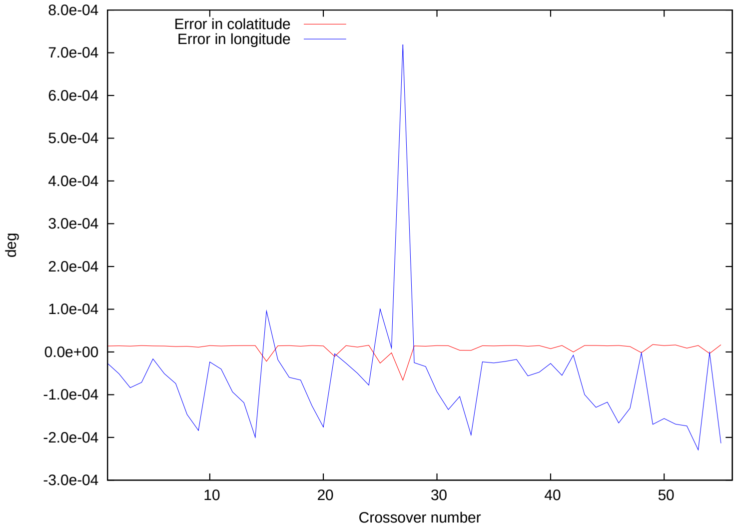

Figure 3.7: Difference in the determination of the colatitude and longitude of the crossovers, between our and DLR software

ing t_1 and t_2, the times corresponding to the intersection of the two ground tracks, the difference in time is of the order of 10^{-4} s both for t_1 and t_2. The colatitude of crossovers is computed with a difference of the order of 10^{-5} degree, while it is slightly larger for the longitude, due to the proximity to the pole, where the longitude is rapidly changing. In terms of meters on the surface, the difference ranges between 50 cm and 1 m.

Finally, when the crossover is correctly detected, the observable for the orbit determination process must be computed. The crossover observable is the difference between the laser altimeter measurements at t_1 and t_2:

$$CO = LA(t_1) - LA(t_2). \tag{3.6}$$

Clearly, it is unlikely that the laser altimeter measurements have been taken exactly at the required times. On the other hand, one can compute the distance between two consecutive readings of the laser altimeter and the dimension of the footprint, in order to verify whether a linear interpolation is allowed. Considering the nominal frequency of 10 Hz and a beam divergence of 50 μrad (full angle), at the minimum altitude (400 km) the distance between two laser measurements is about 260 m and the footprint has a diameter of 20 m, while at the maximum altitude (1000 km) the distance is 180 m, and the diameter is 50 m. Since the measurement of the laser altimeter is representative of the area covered by its footprint, a linear interpolation between the two closest laser altimeter readings around t_1 and t_2 is considered a feasible solution in order to compute the value of the observable (eq. 3.6) (Shum et al., 1990).

3.3.3 *Partial derivatives computation*

Crossover observables have to be included in the orbit determination process, together with Doppler and range measurements, in order to carry out estimation processes exploiting the information of all these different kinds of observables. The least square filter software developed in our laboratory has the capability to accept new kinds of observables, provided that the partial derivatives of these observables with respect to all the solve-for parameters are computed and provided to the code.

In this paragraph we report on the computation of partial derivatives for crossover observables, while in the next we give a general view of the complete process of simulation and estimation and we focus on the use of crossover in a multiarc estimation.

Being $\mathbf{p}$ the vector of parameters we want to estimate, it is possible to distinguish between the state vector $\mathbf{s}$, containing the position and velocity components of the spacecraft, and all the other dynamical model parameters $\mathbf{q}$:

$$\mathbf{p} = \begin{pmatrix} \mathbf{s} \\ \mathbf{q} \end{pmatrix}. \tag{3.7}$$

The crossover observable is the difference between the distances of the spacecraft from the planet's surface at the point where the two ground tracks intersect, $h(t_1)$ and $h(t_2)$. If the crossover location is correct, the topography of the sub-satellite point is the same at t_1 and t_2 and can be expressed as $T(\theta, \lambda)$, so $h(t)$ can be expressed as difference between the distance of the spacecraft from the center of the planet $r(t)$ and the topography:

$$\begin{aligned} z = \Delta h(t_1, t_2) &= h(t_2) - h(t_1) \\ &= [r(t_2) - T(\theta, \lambda)] - [r(t_1) - T(\theta, \lambda)] \\ &= r(t_2) - r(t_1) = f\left(t, \mathbf{s}(\mathbf{q})\right). \end{aligned} \tag{3.8}$$

As it appears clearly in this expression, if the crossover is correctly located, the topography is canceled out in the computation of the predicted observables, assuming that time-varying deformations of the topography are not considered.

We have to compute the partial derivatives of the generic crossover observables $z(t)$ with respect to all the components of the vector $\mathbf{p}$ at the initial time of the estimation arc t_0:

$$\frac{\partial z(t)}{\partial \mathbf{p}(t_0)} = \begin{pmatrix} \dfrac{\partial z(t)}{\partial \mathbf{s}(t_0)} \\ \dfrac{\partial z(t)}{\partial \mathbf{q}} \end{pmatrix}. \tag{3.9}$$

Thanks to the chain rule in the computation of partial derivatives, we can write:

$$\frac{\partial z(t)}{\partial \mathbf{s}(t_0)} = \frac{\partial z(t)}{\partial \mathbf{s}(t)} \frac{\partial \mathbf{s}(t)}{\partial \mathbf{s}(t_0)} \tag{3.10}$$

$$\frac{\partial z(t)}{\partial \mathbf{q}} = \frac{\partial z(t)}{\partial \mathbf{s}(t)} \frac{\partial \mathbf{s}(t)}{\partial \mathbf{q}}. \tag{3.11}$$

Considering the expression of crossover observables in equation 3.8, the partial derivatives are:

$$\frac{\partial z(t)}{\partial \mathbf{s}(t_0)} = \frac{\partial\left(r(t_2)-r(t_1)\right)}{\partial \mathbf{s}(t_0)} = \frac{\partial r(t_2)}{\partial \mathbf{s}(t_0)} - \frac{\partial r(t_1)}{\partial \mathbf{s}(t_0)} \tag{3.12}$$

$$= \frac{\partial r(t_2)}{\partial \mathbf{s}(t_2)}\frac{\partial \mathbf{s}(t_2)}{\partial \mathbf{s}(t_0)} - \frac{\partial r(t_1)}{\partial \mathbf{s}(t_1)}\frac{\partial \mathbf{s}(t_1)}{\partial \mathbf{s}(t_0)}, \tag{3.13}$$

$$\frac{\partial z(t)}{\partial \mathbf{q}} = \frac{\partial\left(r(t_2)-r(t_1)\right)}{\partial \mathbf{q}} = \frac{\partial r(t_2)}{\partial \mathbf{q}} - \frac{\partial r(t_1)}{\partial \mathbf{q}} \tag{3.14}$$

$$= \frac{\partial r(t_2)}{\partial \mathbf{s}(t_2)}\frac{\partial \mathbf{s}(t_2)}{\partial \mathbf{q}} - \frac{\partial r(t_1)}{\partial \mathbf{s}(t_1)}\frac{\partial \mathbf{s}(t_1)}{\partial \mathbf{q}}. \tag{3.15}$$

Defining:

$$\mathbf{A}(t) = \frac{\partial r(t)}{\partial \mathbf{s}(t)}, \qquad \underline{\mathbf{U}}(t) = \frac{\partial \mathbf{s}(t)}{\partial \mathbf{s}(t_0)}, \qquad \underline{\mathbf{V}}(t) = \frac{\partial \mathbf{s}(t)}{\partial \mathbf{q}}, \tag{3.16}$$

we can finally express the partial derivatives of crossover observable as:

$$\frac{\partial z(t)}{\partial \mathbf{p}(t_0)} = \begin{pmatrix} \dfrac{\partial z(t)}{\partial \mathbf{s}(t_0)} \\[2ex] \dfrac{\partial z(t)}{\partial \mathbf{q}} \end{pmatrix} = \begin{pmatrix} \mathbf{A}(t_2)\underline{\mathbf{U}}(t_2) - \mathbf{A}(t_1)\underline{\mathbf{U}}(t_1) \\[2ex] \mathbf{A}(t_2)\underline{\mathbf{V}}(t_2) - \mathbf{A}(t_1)\underline{\mathbf{V}}(t_1) \end{pmatrix}. \tag{3.17}$$

$\mathbf{A}(t)$ can be easily computed, considering $r(t) = \sqrt{(x^2+y^2+z^2)}$; therefore, $\mathbf{A}(t)$ is a vector of six parameters, with the last three equal to zero, because the partial derivatives of $r(t)$ with respect to the component of the velocity of the spacecraft are null.

$\underline{\mathbf{U}}(t)$ and $\underline{\mathbf{V}}(t)$ are part of the transition matrix $\Phi(t, t_0)$, and are stored in a binary file, generated by ODP, during the spacecraft trajectory propagation (Moyer, 1971).

3.3.4 *Integration of crossover observables in orbit determination process*

The last step to use crossover observables in the orbit determination process is the inclusion of the partial derivatives in the mapping matrix **H** and the computation of residuals, as differences between observed (or simulated) observables and computed observables. Before focusing on the structure of the mapping matrix, we give an overview of the complete process carried out in the numerical simulations.

With an appropriate setup (see paragraph 2.2) we can propagate a simulated trajectory, corresponding to the true, unknown trajec-

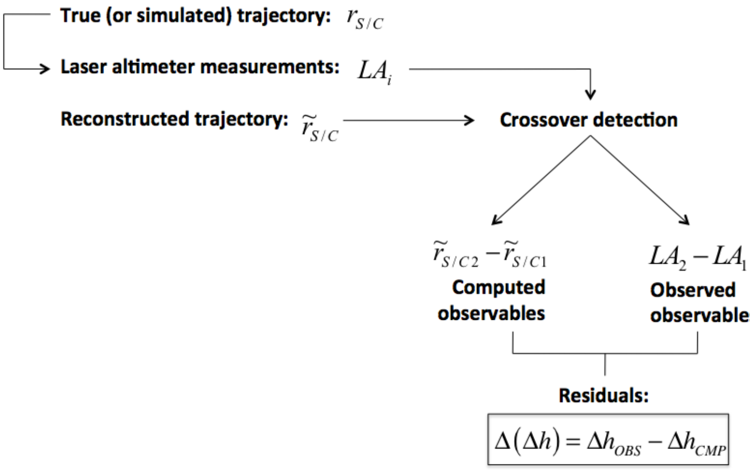

Figure 3.8: Simulation and estimation process with crossover observables

tory we want to reconstruct when we analyze real data. With respect to this trajectory, we can generate our simulated observables (e.g. Doppler, range and crossovers), that represent the real data collected by the spacecraft instruments. On the other side, either if we are using simulated data or if we collect real data, we have an initial guess of the spacecraft's initial conditions and of the dynamical model parameters needed to represent all the forces acting on the spacecraft. Therefore, we can generate a reconstructed trajectory, and we can use this trajectory to compute the expected value of the observables. With the iterative estimation process, we want to move this reconstructed trajectory as closest as possible to the simulated (or true) one, by residuals minimization.

Focusing on crossover observables (see figure 3.8), we can use the simulated trajectory to generate laser altimeter measurements. Then, considering the reference trajectory of the estimation process, we can detect crossovers, and compute residuals and partial derivatives (as explained in section 3.3.3). In particular, being t_1 and t_2 the times of the crossover, the simulated (or observed) observable is $LA(t_2) - LA(t_1)$, while the computed observables is $r(t_2) - r(t_1)$, where $r(t)$ is the distance between the spacecraft and the planet's surface. It is important to note that, in this way, the knowledge of the topography of the planet is not required, because its value is cancelled in the subtraction. Residuals will tend to zero if time-varying topography deformation are not taken into account, or to the expected value of such deformation in the time interval between the two laser altimeter measurements of the crossover. In any case, this can introduce an important error if the crossover is not accurately detected.

In a classic batch estimation, it is easy to include crossover observables in the orbit determination process. In fact, it is sufficient to add these observables to the measurements vector (equation 2.4), and the correspondent partial derivatives with respect to the solve-for parameters in the mapping matrix **H**. The problem can be solved by using equation 2.15.

Some complications arise if we want to carry out a multiarc estimation (see paragraph 2.3.2). Therefore, there is not a single reference epoch, but as many as the number of arcs. It means that we have to compute partial derivatives of an observable with respect to the initial state of the arc in which that observable occurs. Now we need to distiguish between intra-arc and inter-arc observables.

If we consider only radio measurements, the mapping matrix has the structure shown in equation 2.22: Doppler and range observables have a single timetag, so there will be only partial derivatives of such observables with respect to the local parameters of the corresponding arc, and, obviously, with respect to the global parameters.

On the other hand, crossover observables are identified by two different times (t_1 and t_2). If t_1 and t_2 are contained in the same arc, there are no differences with Doppler and range observables: it is an intra-arc observable and we can compute partial derivatives with respect to the local parameters of that arc, and with respect to the global parameters. But, it can happen that t_1 and t_2 belong to different arcs. In this case, the structure of the mapping matrix needs to be modified because, in addition to the partial derivatives with respect to global parameters, there will be the partial derivatives with respect to two different set of local parameters, respectively corresponding to the two involved arcs.

Let's consider again the case with three different arcs. Being $\mathbf{z}_i$ the vector of radio observables of the i^{th} arc, while w_1 is a single crossover observable with t_1 and t_2 occurring respectively in the first and in the third arc, and w_2 another crossover with t_1 and t_2 in the second and in the third. The mapping matrix will be:

$$\mathbf{H} = \begin{pmatrix} \dfrac{\partial \mathbf{z}_1}{\partial \mathbf{l}_1} & 0 & 0 & \dfrac{\partial \mathbf{z}_1}{\partial \mathbf{g}} \\ 0 & \dfrac{\partial \mathbf{z}_2}{\partial \mathbf{l}_2} & 0 & \dfrac{\partial \mathbf{z}_2}{\partial \mathbf{g}} \\ 0 & 0 & \dfrac{\partial \mathbf{z}_3}{\partial \mathbf{l}_3} & \dfrac{\partial \mathbf{z}_3}{\partial \mathbf{g}} \\ \dfrac{\partial w_1}{\partial \mathbf{l}_1} & 0 & \dfrac{\partial w_1}{\partial \mathbf{l}_3} & \dfrac{\partial w_1}{\partial \mathbf{g}} \\ 0 & \dfrac{\partial w_2}{\partial \mathbf{l}_2} & \dfrac{\partial w_2}{\partial \mathbf{l}_3} & \dfrac{\partial w_2}{\partial \mathbf{g}} \end{pmatrix} \tag{3.18}$$

and the problem can be again solved with the equation 2.15.

The least square filter code, developed in our laboratory, has the capability to include new observables, providing the necessary partial derivatives, but it was able to process only matrices with a single block of partial derivatives with respect to local parameters (as in equation 2.22). The QR factorization of the mapping matrix (see paragraph 2.3.1) is, in fact, realized by means the triangularization of the different parts of the matrix, containing only the observables of a single arc. In this way, the process can be parallelized and speeded up. Unfortunately, this triangularization method works only with matrices with the structure reported in equation 2.22. Therefore, in order to include crossover observables in a multiarc estimation, it has been necessary to modify the code, adding the possibility to handle mapping matrices with two blocks of partial derivatives with respect to local parameters of two arcs (as in equation 3.18).

A simplified scheme of the initial structure of the estimation filter is shown in figure 3.9: the software was able to manage as input the regres.nio files, that are binary files generated by the ODP, where Doppler and range observables are stored, together with their residuals and partial derivatives. Thanks to a parallel processing, the software builds the triangular matrix $\mathbf{R_1}$ and solves the orbit determination problem, providing as output the estimated values of the spacecraft initial conditions and the other required parameters, and the associate covariance matrix.

The figure 3.10 shows the modified structure of the code. The processing flux relative to the radio observables is not changed, but it

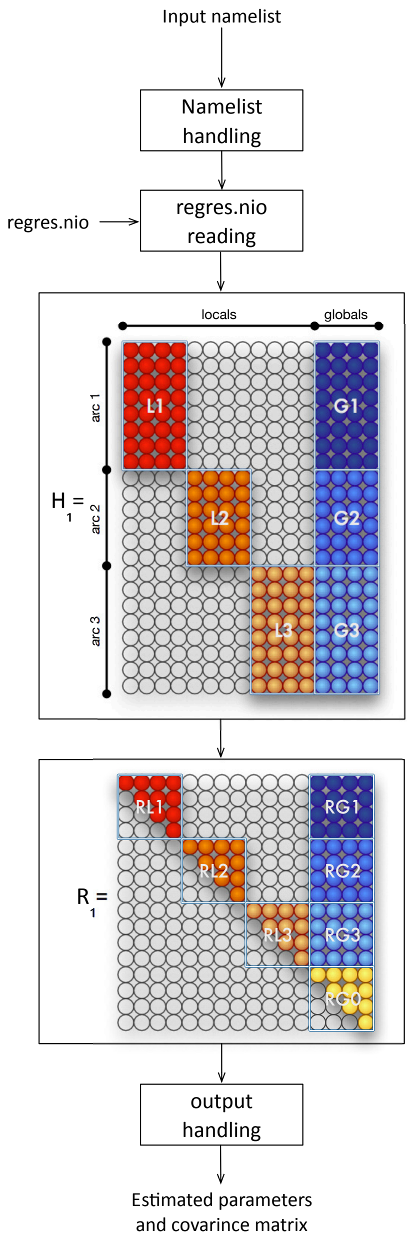

Figure 3.9: Structure of the least square filter code, using only intra-arc observables

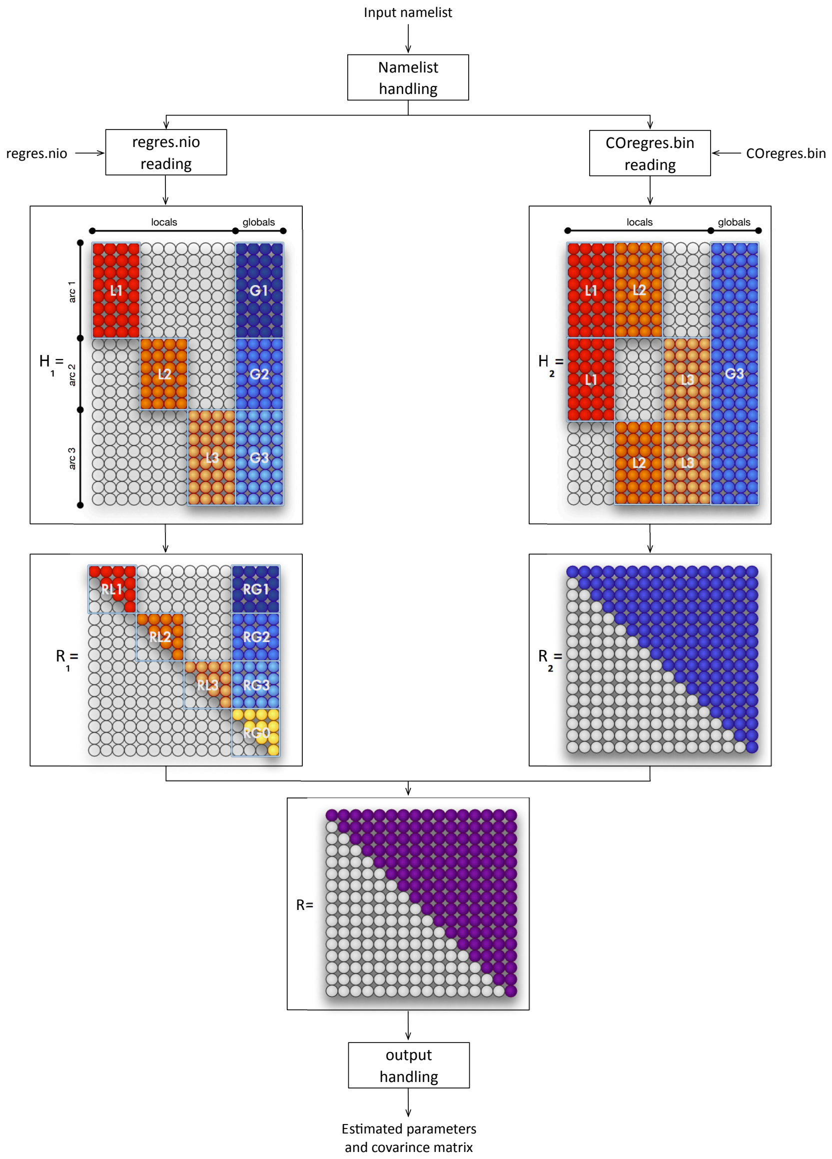

Figure 3.10: Structure of the least square filter code, using both intra-arc and inter-arc observables

is accompanied by an additive part specifically developed to handle inter-arc observables, with partial derivatives with respect to two sets of local parameters. Crossover observables, residuals and partial derivatives are stored in COregres.bin files, generated by the code developed to compute crossover partial derivatives. A check over t_1 and t_2 and the initial times of the considered arcs is performed in order to correctly insert the partial derivatives in the corresponding block of local parameters in the mapping matrix $\mathbf{H_2}$. The triangular matrix $\mathbf{R_2}$ is then computed without parallelization. Finally, the two triangular matrix $\mathbf{R_1}$ and $\mathbf{R_2}$, obtained respectively with radio observables and crossover, are joined by means of another QR factorization. Estimated values and associated covariance matrix are therefore computed by exploiting the information content of both radio and crossover observables.

In the following chapter, we report on the results of numerical simulations carried out with and without crossover observables, in order to draw some conclusions regarding the contribution of crossover in the case of the BepiColombo radioscience experiment.

4

NUMERICAL SIMULATIONS

In this chapter we summarize the results of the numerical simulations carried out to evaluate the contribution of crossover observables in the determination process, in the context of the BepiColombo radio science experiment.

In order to point out this contribution, we first considered a reference case, with radio observables, only. The Doppler and range accuracy is set equal to the foreseen accuracy of BepiColombo MORE data (MORE Team, 2011) while the simulation setup is slightly simplified with respect to the one reported in 2.2.

Later, we added crossover observables and carried out analogue numerical simulations, including both radio and crossover observables, using different values of crossover observables weights in the weighted least square solution, so that we can immediately compare the results with the reference case.

Finally, as last check of our results, a setup with only X band data has been considered, in order to verify the possible improvement in the estimation when crossovers are added to less accurate radio data.

4.1 REFERENCE CASE

This reference case is the term of comparison necessary to evaluate the contribution of crossover observables. In this paragraph we report on the results obtained in this case, in terms of gravity field harmonic coefficients estimation and spacecraft trajectory reconstruction.

On the base of the simulation setup reported in 2.2, some simplifications have been done, because here the aim is no more to verify the attainable accuracy of the radio science experiment, that therefore requires a setup as much realistic as possible, but to evaluate whether or not crossover observables can improve the estimation process, when

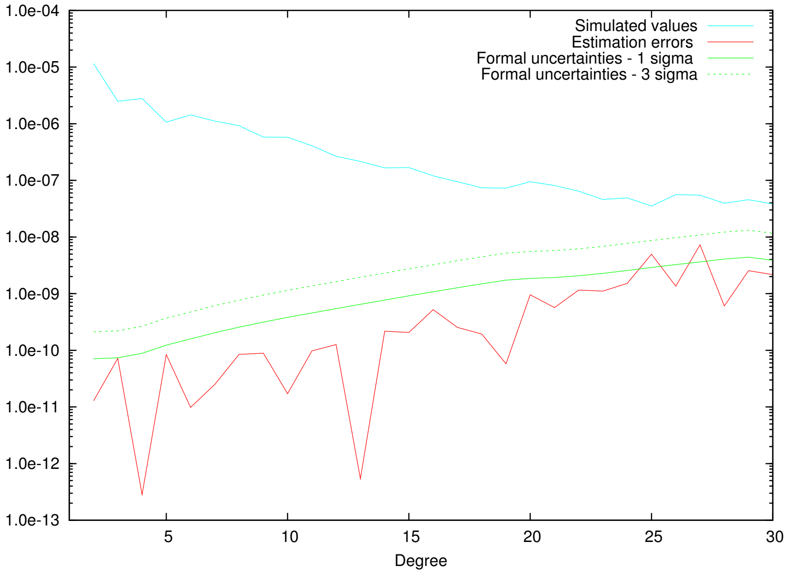

Figure 4.1: Estimated gravity field (reference case)

a novel and extremely accurate tracking system is available, as in the case of the radio science experiment onboard BepiColombo mission.

In particular, desaturation maneuvers are not implemented, unlike in the realistic case, the accelerometer is supposed to correctly remove all the non gravitational accelerations, and the accelerometer noise is not added in the model. The main difference between the dynamical model used to simulate Doppler and range observables and the model used in the estimation process concerns the Mercury's gravity field: in the first model, the coefficients of the spherical harmonic expansion are taken from MESSENGER team estimation (Smith et al., 2012), while in the estimation model the values are slightly different, with a priori uncertainties that contain the true values.

The estimation process has been carried out with a sequential batch filter (see paragraph 2.3.3). We considered 5 batches of 22 arcs each one, for a total of two Mercury days.

We avoid to report here the partial results of the multiarc estimation that follows each batch (step I in figure 2.3), because the first step of the sequential batch estimation is only needed to reconstruct a good trajectory, by means of consecutive updates of the dynamical model. This reconstructed trajectory is later used to retrieve the gravity field coefficients, and global parameters in general, in the complete multiarc estimation (see step II in figure 2.3).

The estimated gravity field coefficients obtained with the complete multiarc estimation is our best gravity field estimation and it is shown in figure 4.1. On the x-axis there are the degrees of the spherical harmonic expansion and their value is computed as the sum of all coefficients of that degree, according to the following expression:

$$C_l = \sqrt{\frac{1}{2l+1}\sum_m (C_{lm}^2 + S_{lm}^2)}. \tag{4.1}$$

The blue line represents the simulated values of the gravity field coefficients. The red line is the estimation error, that is the difference between the estimated and the simulated values. The green solid line represents the formal uncertainty associated to the estimated value, while the green dotted line is three times such uncertainty (3-σ level).

The main advantage of numerical simulations is the knowledge of the true value of each parameter of interest. In this way, it is easy to check the correctness of the estimate. The estimation error, in fact, should be smaller than the associated formal uncertainty. Estimation error under the 3-σ level are statistically acceptable, as well.

The figure 4.1 shows a fairly good estimation of the gravity field coefficients. Almost all degrees are determined with an estimation error smaller than the associated formal uncertainty, meaning that the simulated true value is included within the uncertainty. Only a couple of high degrees have estimation errors that exceed the formal uncertainties, but are well below the 3-σ level.

Furthermore, it is important to look at the ratio between the value of the coefficient and its uncertainty. The goals of the radio science experiment foresee a signal to noise ratio of $\approx 10^4$ for the degree 2, of ≈ 300 for degree 10 and ≈ 10 for the higher degree (see section 2.1). The estimate carried out shows clearly that all these goals are reached and, sometimes, exceeded.

Finally, we can look at the Ka band Doppler residuals of the multi-arc solution at the Goldstone antenna (figure 4.2), for a last check of the estimate. Residuals are zero mean and do not show any kind of signatures. Moreover, the residuals RMS of 1.3 10^{-3}Hz is equal to the RMS of the white Gaussian noise added on the simulated observables (see paragraph 2.2).

As explained in paragraph 2.3.3, the estimated gravity field and its associated formal uncertainties are input in the last step of the estimation process, needed to recover the spacecraft trajectory with an improved accuracy, thanks to the better dynamical model.

The output of this last step is, therefore, the estimation of position and velocity vectors of the spacecraft at the initial time of each arc. In the figures 4.3 and 4.4, the estimation errors and the formal uncertainties (3-σ) are shown, with solid and dotted lines respectively, in the radial direction R, in the transversal direction T (perpendicular

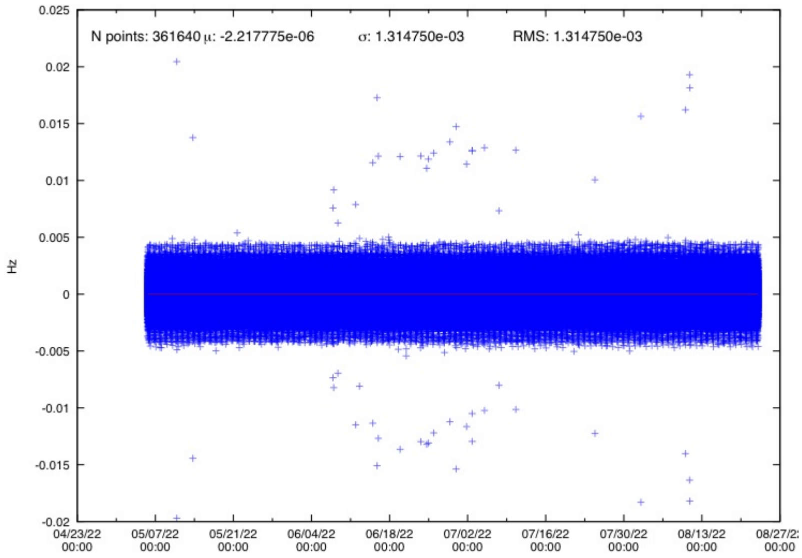

Figure 4.2: Ka-band Doppler residuals of multiarc solution (reference case)

	R	T	H
Estimation error (m)	0.012	0.055	0.081
Formal uncertainties (m)	0.016	4.459	5.591

Table 4.1: Mean values of estimation errors and formal uncertainties for the spacecraft position components

to the radial and lying in the orbital plane) and in the out of plane direction H. Again, being a simulation, we have the opportunity to verify that the estimation errors are always below the 3-σ level of formal uncertainties, attaining a confirmation of the correctness of the estimation.

The mean values of estimation errors and the associated formal uncertainties (1-σ) are summarized in table 4.1. The accuracy in the determination of the radial component of the spacecraft position is two orders of magnitude better than the other two directions, and this is a usual result in orbiter position determination. Anyway, we need to stress that, even if the other two directions have larger formal uncertainties, the knowledge of the simulated trajectory provides us the opportunity to observe that the estimation errors in T and H directions are less than 10 cm.

The reconstruction of the MPO trajectory is necessary to retrieve Mercury's topography, with laser altimeter data. In fact, the laser altimeter measures the distance between the spacecraft and the surface of the planet, by means of the time of flight of a laser pulse. Therefore

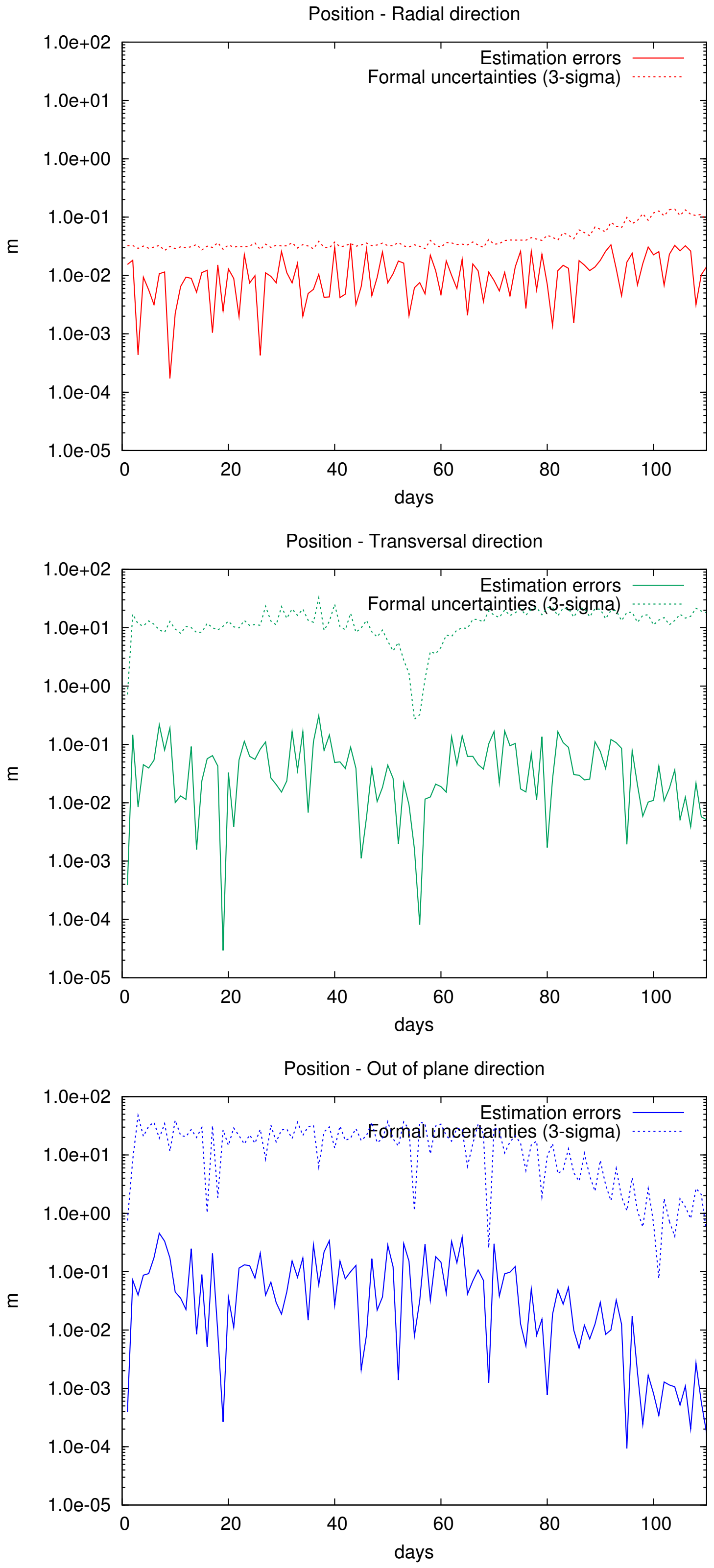

Figure 4.3: Estimation errors and formal uncertainties (3-σ) in the three component of the spacecraft position

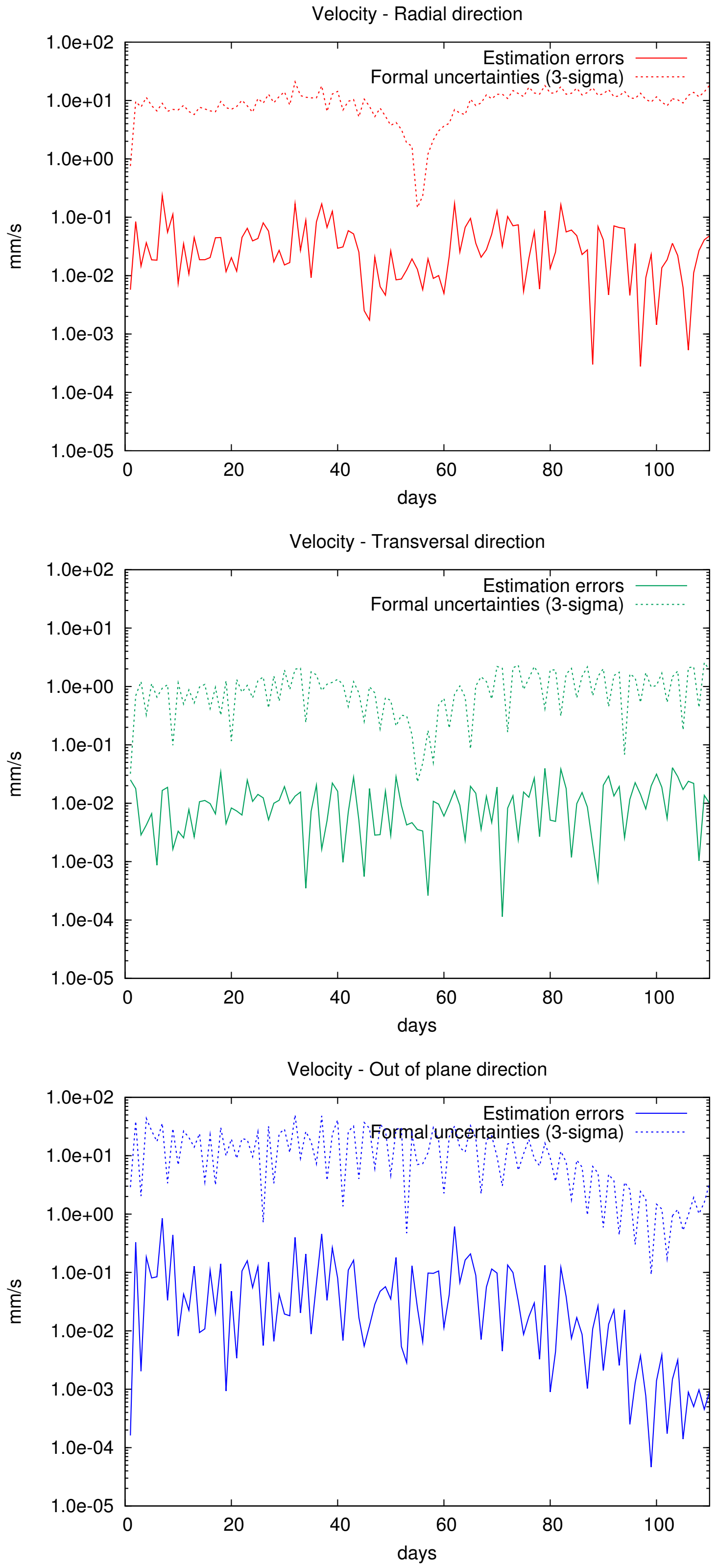

Figure 4.4: Estimation errors and formal uncertainties (3-σ) in the three component of the spacecraft velocity

the precise knowledge of the spacecraft position has an immediate positive outcome on the accuracy of the topography of the planet.

4.2 RADIO AND CROSSOVER OBSERVABLES CASE

In this section we report on numerical simulations carried out with both radio and crossover observables. The simulation setup is the same used in the reference case and reported in the previous paragraph. The method used to simulate laser altimeter measurements, to detect crossovers and to compute residuals and partial derivatives of crossover observables is described in the chapter 3.

Being a simplified case, the noise added on the simulated laser altimeter measurements does not take into account nadir pointing and slope contribution, as in the expression 3.5; only white Gaussian noise with an RMS of 30 cm has been added.

Some checks have been necessary to investigate the work done to include crossover observables in the orbit determination process, and in case to correct possible errors and bugs. We will first summarize these checks and later show our results.

4.2.1 *Verifications*

The first check we performed concerns the formal uncertainties associated to the estimated values: the information matrix is defined as positive definite, so when new observations are added, the information content increases. Therefore, the formal uncertainties, equal to the square root of the diagonal elements of the covariance matrix, obtained by the inversion of the information matrix, result smaller than before (Tapley et al., 2004).

By comparing two estimates, respectively with and without crossover observables, we can verify that the formal uncertainties are lower when crossovers are added to the radio data. We considered here the first arc of the first batch, because in this way the a priori covariance matrix used is the same, since it does not come from a propagation of a previous estimation, but it is part of the initial guess. With only 55 crossover observables added to the information matrix, the decrease of the formal uncertainties for both local and global parameters can be noticed.

In the table 4.2 we reported the formal uncertainties associated to the spacecraft state vector components, when the estimation is carried out with radio measurements only and when also crossovers are included. The last column of the table is the percentage varia-

Formal uncertainties	Only radio observables	Radio and crossovers	Percentage variation
X (m)	0.519489	0.519484	-0.0086
Y (m)	0.300125	0.300104	-0.0686
Z (m)	0.207545	0.207509	-0.1722
DX (mm/s)	0.883552	0.883551	-0.0020
DY (mm/s)	0.345855	0.345826	-0.0820
DZ (mm/s)	0.385653	0.385577	-0.1989

Table 4.2: State vector component formal uncertainties of the first arc, obtained with only radio observables and with both radio and crossover, and their percentage variation

tion with respect to the value obtained without crossover, and it is always negative, meaning that the formal uncertainties obtained with both radio and crossovers are smaller than those obtained with radio measurements only. The minimal variations shown in the table are not significant for evaluating the crossover contribution, since in this case only 55 crossover observables have been added in the estimation process.

Due to the huge number of global parameters (almost 1000), we only report the percentage variation, in the figure 4.5, pointing out that it is always negative.

Therefore, we can confirm that, by adding crossover observables in the information matrix, the formal uncertainties of the estimated parameters decrease.

The second needed check concerns residuals. Being a simulation, we know the value of the noise added on the laser altimeter measurements and we expect to obtain residuals comparable with the noise considered. In this case, we added white Gaussian noise with RMS of 30 cm on simulated laser altimeter observables, while we can only look at the crossover observables residuals. Therefore, we can accept some slight differences, due to the possible error added by the topography, if the crossover is not precisely located.

First simulations show some points with residuals larger than three orders of magnitude with respect to the expected value and a total RMS of 54m, well beyond the acceptable values. To explain and correct this effect, we supposed an error in the crossovers location, producing large residuals because the topography in the two sub-satellite points could be considerably different.

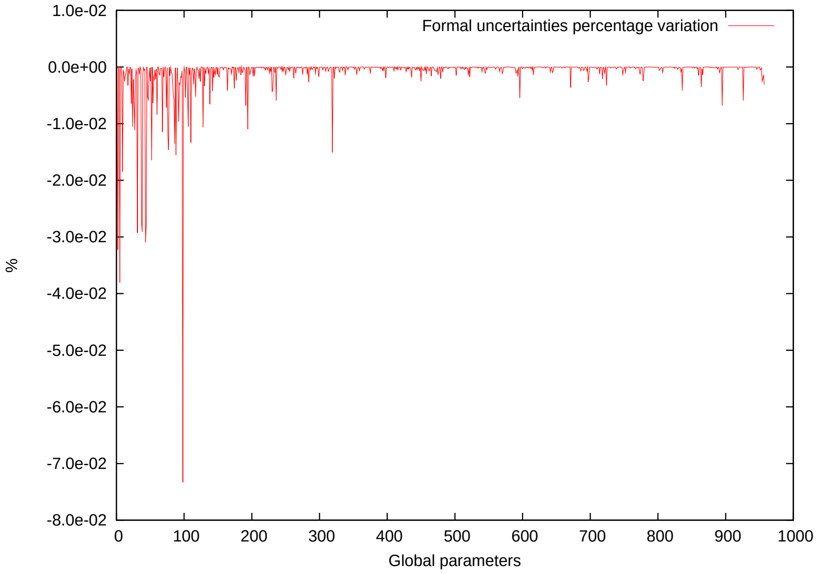

Figure 4.5: Percentage variation of global parameters formal uncertainties obtained with both radio and crossover observables with respect to the case with radio measurements only

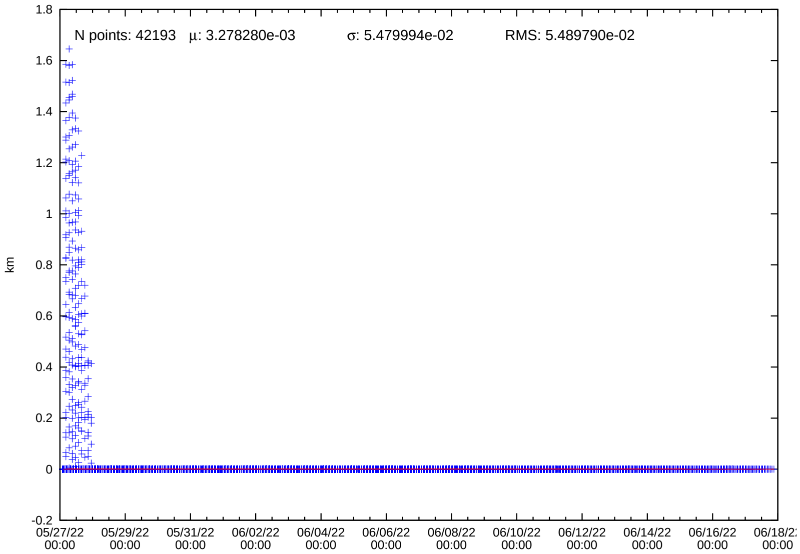

Figure 4.6: Crossover observables residuals of a multiarc estimation of 22 arcs, with outliers

Date	**colat** (deg)	**long** (deg)	r_{SC} (km)	**LA** (km)
27 May 2022 04:22:51	179.81	197.59	3439.51	999.96
29 May 2022 02:52:57	179.81	177.49	3435.35	997.27

Table 4.3: Example of an outlier generated by a wrong crossover location

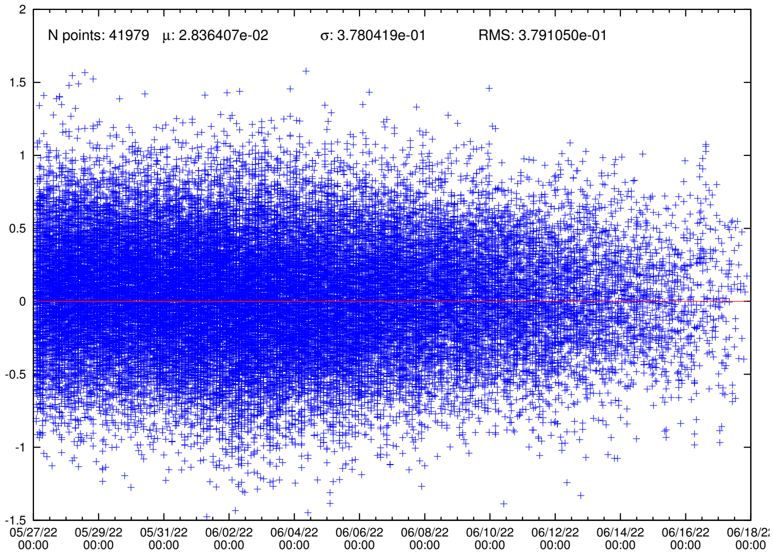

Figure 4.7: Post-fit crossovers residuals of a multiarc estimation of 22 days, after outliers removal

In figure 4.6, crossover residuals of a multiarc analysis of 22 arcs are shown, and the necessity to remove these outliers to avoid biasing the solution is evident. Before removing them, we analyzed some of them, going back to their times and location, in order to verify if the hypothesis of an error in the crossover detection is correct.

We report here an example. One of the points in the figure has a residual of 1.43 km. In table 4.3 we summarized the times of the crossover (t_1 and t_2), the colatitude and longitude, the radial positions of the spacecraft and the laser altimeter readings at the considered times. There are 20° of difference in longitude (corresponding to about 3 km on the surface at that colatitude) and therefore it is not a crossover.

Due to the proximity to the pole, the longitude changes quickly and the detection of crossover by means of linear interpolation of the ground tracks could generate these outliers. The outlier removal has been added in the code, rejecting crossover with pre-fit residuals larger than 100 m or beyond 5 times the RMS value.

Once the outliers are identified, the estimation process can be carried out without using those points. Figure 4.7 shows the post-fit residuals. The RMS is close to 30 cm, as expected, and it is a further confirmation of the correct implementation of crossovers in the orbit determination process.

The crossover residuals have two different reference times, nominally t_1 and t_2. In the plot, we represented residuals using the first time. It clarifies why there are less points at the end of the arc, than at the beginning. Indeed, the initial ground tracks intersect with all the consecutive ground tracks, while in the final part of the trajectory, there are less crossovers.

4.2.2 *Main results*

Before arriving to the results shown in this chapter, several attempts have been necessary, in order to fix or improve different aspects of the whole process.

First of all, the crossover detection software have been modified mainly to decrease the computational time. In fact, it increases about quadratically with the length of the considered trajectory arc. Initially, without parallel processing, the crossover search requested more than three day for a 110 (terrestrial) days arc. Therefore, the parallelization of the code has been implemented, by dividing the ground track in colatitude area and limiting the search inside a single area.

The hypothesis to use portions of ground tracks limited not only in colatitude, but also in longitude have been taken into account, but, after some attempts, it has been discarded. Indeed, close to the poles, the longitude changes so quickly that it could happen to have only a single sample of the ground tracks of some orbits. It made the linear interpolation of such ground tracks impossible, causing the loss of all the crossover formed by that ground track and all the other ones.

Finally, in the last simulations carried out, the computational time needed to detect crossover for a 110 days trajectory was less than 14 hours.

Another important aspect that requested new set of simulations concerns the outliers removal, as explained in the previous paragraph.

We report here the results of the last three numerical simulations, obtained at the end of this improvement process. These cases differ only in the weight of crossover observables. The weighting factor is the square of the reciprocal of a user-assigned crossovers standard deviation. This standard deviation corresponds roughly to the expected crossover discrepancy after adjustment.

Since we did not consider pointing error and surface slope in the computation of the error to be added to the simulated laser altimeter measurements, the expected crossover RMS after adjustment is slightly larger than the RMS of the additive white Gaussian noise. Indeed, crossover are generated by means of two different laser altimeter measurements, each one with its own noise, and possible imprecision in their location could be another error source, due to the topography of the planet.

We used 1 m, 5 m and 10 m as expected standard deviations (σ_z). The weighting factor is computed as the square of the reciprocal of these values:

$$w = \frac{1}{\sigma_z^2}. \tag{4.2}$$

The value of 1 m is considered as the most appropriate for the considered setup, while the other two are used in order to represent the expected value if pointing error and surface slope are considered in the simulation of laser altimeter measurements, and therefore crossover observables have to be deweighted, since the expected noise is larger.

As in the reference case (see paragraph 4.1), the estimation process has been divided into 5 batches of 22 arcs each. For each step of the sequential batch estimation process (see figure 2.3), we compared the obtained results with what we had in the reference case, in terms of estimation errors and formal uncertainties of the spacecraft state vector components at the initial time of each arc. As it is easy to imagine, it is prohibitive to report here all the variations, component by component and arc by arc. Therefore, we will follow here the approach found in the literature: Lemoine et al. (2001) and Mazarico et al. (2011), respectively for MGS and LRO. Those analysis have been realized first with only radio observables and then with both radio and crossovers. Their considered arcs had overlapping periods, and the estimates variation has been reported as the mean value of the overlap discrepancies, in the three components of the spacecraft position.

Basically, with real data, the overlap discrepancy is more significant than the formal uncertainty. With the true values unknown, it is impossible to check whether the estimation error is below the uncertainty threshold. Therefore, the overlap discrepancy can be assumed as the best knowledge of the true value. Our setup does not foresee any overlaps, but, being a simulation, we can check the estimation error, and we will report the mean value of the formal uncertainties.

It is important to note that, due to the complexity of the process, it is not taken for granted that all formal uncertainties decrease by adding new observables in this case. Indeed, two different contributions flow into the covariance matrix: the information matrix, with the observables content, and the a priori covariance matrix. If the apriori covariance matrix was the same, the formal uncertainties would be reduced when new observables are included in the estimation, as verified in paragraph 4.2.1. In the sequential batch estimation, the estimated values of the initial conditions of one arc are propagated to the initial time of the following arc, and the associated covariance matrix is mapped at that time and used as apriori information. In addition, also the estimated global parameters and their formal uncertainties obtained in the multiarc analysis of one batch are used in the dynamical model of the following batch, as nominal values and apriori covariance. Therefore, it is impossible to distinguish between the two contributions of the covariance matrix, but we can have an overall view of the estimation.

In the table 4.4, we report the mean values of the (3-σ) formal uncertainties associated to the three components of the spacecraft position vector, for the five multiarc estimations of the first step of the batch sequential process (see step I in figure 2.3), both for the reference case and the three cases with radio and crossover observables. Both intra-arc crossovers (formed from intersecting orbits within a single arc) and inter-arc crossovers (formed from intersecting orbits that occur in different arcs) have been included.

When, adding crossovers, the formal uncertainties decrease with respect to the corresponding values of the reference case, the value is written in bold type, in order to improve the immediate readability of the table. In general, in the simulation with $\sigma_w = 1$ m, we always have a reduction of the formal uncertainties, from few centimeters up to 1 m. The ratio between the estimated values and the associated formal uncertainties has been computed but it shows such little differences that we decided to avoid reporting here an analogous table with estimation errors.

Then, we considered the complete multiarc estimation (see step II in in figure 2.3) and we report in table 4.5 the mean value of the position components formal uncertainties. In this case, we have a decrease of a few centimeters in the estimate with $\sigma_w = 1$ m, while in the other two cases the difference is exiguous.

We also investigated the global parameters estimation, even if, given the small variation in the local parameters, we do not expect any significant changes. Figure 4.8 shows the estimation errors and the associated formal uncertainties of the gravity field coefficients, both for the reference case and the three case with radio and crossover observables. As expected, the difference in the formal uncertainties are not remarkable (< 0.1 mGal), while the estimation errors show some vari-

Ka-band		**Formal uncertainties**		
		X (m)	Y (m)	Z (m)
Batch 1	Without crossover	20.989	9.829	8.626
	With crossover σ_w =1 m	**20.945**	**9.808**	**8.607**
	With crossover σ_w =5 m	20.992	9.831	8.627
	With crossover σ_w =10 m	20.990	9.830	8.627
Batch 2	Without crossover	17.143	9.512	9.482
	With crossover σ_w =1 m	**16.990**	**9.427**	**9.393**
	With crossover σ_w =5 m	**17.133**	**9.506**	**9.478**
	With crossover σ_w =10 m	17.162	9.522	9.489
Batch 3	Without crossover	16.862	3.705	4.819
	With crossover σ_w =1 m	**16.247**	**3.571**	**4.615**
	With crossover σ_w =5 m	16.930	3.720	4.835
	With crossover σ_w =10 m	16.906	3.715	4.830
Batch 4	Without crossover	16.417	11.419	13.020
	With crossover σ_w =1 m	**15.230**	**10.406**	**11.923**
	With crossover σ_w =5 m	16.439	11.419	13.024
	With crossover σ_w =10 m	16.472	11.457	13.063
Batch 5	Without crossover	4.468	12.852	14.101
	With crossover σ_w =1 m	**4.177**	**12.048**	**13.204**
	With crossover σ_w =5 m	**4.447**	**12.780**	**14.026**
	With crossover σ_w =10 m	4.471	12.855	14.105

Table 4.4: Multiarc estimation of the batches: mean value of position formal uncertainties

Multiarc	**Formal uncertainties**		
	X (m)	Y (m)	Z (m)
Without crossover	3.416	1.790	1.786
With crossover σ_w =1 m	**3.328**	**1.739**	**1.736**
With crossover σ_w =5 m	**3.411**	**1.787**	**1.783**
With crossover σ_w =10 m	3.416	1.791	1.786

Table 4.5: Complete multiarc estimation: mean values of position formal uncertainties

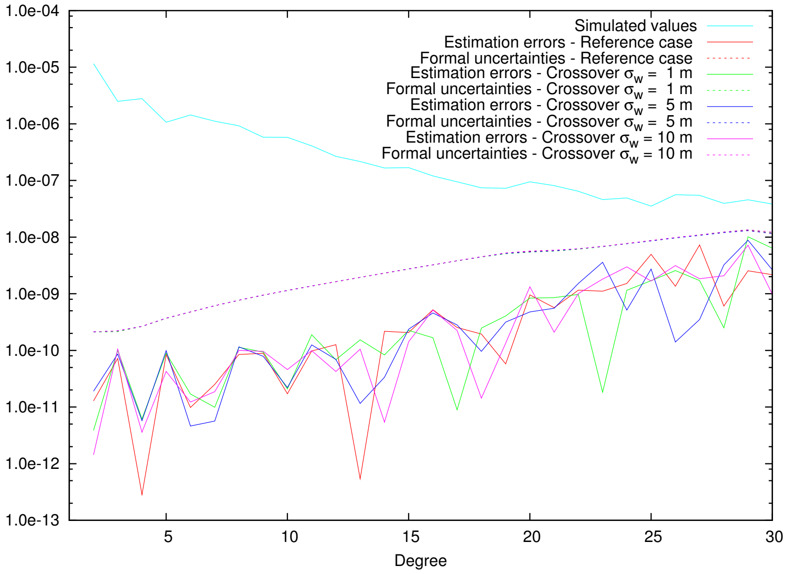

Figure 4.8: Multiarc: estimation errors and formal uncertainties of the gravity field coefficients

Last step	**Formal uncertainties**		
	R (m)	T (m)	H (m)
Without crossover	0.0476	13.377	16.772
With crossover σ_w =1 m	**0.0474**	**13.332**	**16.732**
With crossover σ_w =5 m	**0.0476**	13.386	16.798
With crossover σ_w =10 m	0.0476	13.404	16.813

Table 4.6: Last step: position formal uncertainties

ations, even if they have the same behavior and always lie below the 3 sigma level.

Finally, in table 4.6 we report the formal uncertainties variation for the last step of the sequential batch process (see step III in in figure 2.3). Here the position components are rotated in radial (R), transversal (T) and out of plane (H) components. The reduction is again of the order of a few centimeters, even if only about 55 crossovers are added in each arc, being single arc estimations.

4.2.3 *Literature and X-band case*

The previous paragraph has shown how an improvement of a few centimeters in the determination of the spacecraft position can be achieved by adding crossover observables in the estimation process for the BepiColombo radio science experiment, considering a simplified setup and error model for laser altimeter measurements. It is not surprisingly, due to the intrinsic accuracy of Doppler and range measurements, provided by the advanced Ka-band radio system, and the plasma and troposphere effects cancellation, by means, respectively, of the multifrequency system and the water vapor radiometer.

Past experiences reported in literature show well more significant improvements, but the analyzed mission configuration were different from BepiColombo.

In Mazarico et al. (2011), the results of the orbit determination from the radio science investigation of the Lunar Reconnaissance Orbiter (LRO) are reported. LRO was designed to provide a comprehensive and detailed survey of the Moon and was launched on June 2009. LRO was tracked anytime it was visible from one of the ground network stations: a new LRO-dedicated NASA station in White Sands, New Mexico, and the commercial Universal Space Network (USN). All of those stations produce S-band Doppler and range radiometric data and the data are then corrected for tropospheric delays from

LRO	**Orbit overlap**		
	R (m)	T (m)	H (m)
Without crossover	4.50	49.90	47.57
With crossover	**3.96**	**14.26**	**17.22**

Table 4.7: LRO: orbit overlaps (with GLGM-3 model as apriori)

LRO	**Orbit overlap**		
	R (m)	T (m)	H (m)
Without crossover	1.58	15.44	16.71
With crossover	1.80	**8.37**	**10.18**

Table 4.8: LRO: orbit overlaps (with LLGM-1 model as apriori)

meteorological information collected at the stations. The radiometric tracking performance was ≈ 0.3 mm/s and ≈ 0.2 m for White Sands, and ≈ 0.4 - ≈ 0.8 mm/s and ≈ 0.4 m for USN.

LOLA is the onboard Lunar Orbiter Laser Altimeter, a 10 cm precision 28 Hz, five-beam laser altimeter, described in detail by Smith et al. (2009).

In the orbit determination process the quality of the orbits has been assessed primarily through overlap analysis, that is the consistency of trajectory segments when processed in two consecutive time periods. The estimation process has been carried out with only radio observables and later, crossovers have been added. Table 4.7 reports the average overlap RMS differences, when the gravity field GLGM-3 is used as apriori. GLGM-3 is the solution of the reprocessing at NASA GSFC of historical lunar tracking data, as Lunar Orbiters, Apollo sub-satellites, Clementine and Lunar Prospector, in preparation for the LRO orbit determination effort (Mazarico et al., 2010). Thanks to crossovers, the overall overlap RMS values decrease from ≈ 70 m in total position to ≈ 23 m, a 70% of reduction.

After the determination of a new gravity model (LLGM-1, LRO Lunar Gravity Model), the orbit determination process is repeated with radio observables and with both radio and crossovers. The average overlap in the spacecraft position reconstruction is summarized in table 4.8. The relative improvement is much smaller than the previous case, but still significant (19%).

In Lemoine et al. (2001), an improved harmonic solution of the Mars gravity field to degree and order 80 is presented. GGM-2B (Goddard Mars Model 2B) has been obtained by using X band tracking

MGS	**Orbit overlap**		
	R (m)	T (m)	H (m)
Without crossover	0.08	12.3	0.56
With crossover	**0.05**	**5.64**	**0.27**

Table 4.9: MGS: orbit overlaps (GCO phase)

MGS	**Orbit overlap**		
	R (m)	T (m)	H (m)
Without crossover	1.02	2.56	8.69
With crossover	1.05	2.55	8.75

Table 4.10: MGS: orbit overlaps (mapping phase)

data of Mars Global Surveyor (MGS), from October 1997 to February 2000, and altimeter crossovers formed from the Mars Orbiter Laser Altimeter (MOLA) data between March and December 1999. The X-band frequency used on MGS is less sensitive to noise and disturbances from the Earth troposphere and solar plasma than the S band frequency of the previous generation of Mars Orbiters. MGS achieved a data noise of 0.1 mm/s over a 10 s counting interval.

MGS orbit determination has been carried out with radio data and both radio and crossovers, for two different phases of the mission: the gravity calibration orbit (GCO), and the mapping phase. The GCO period (about three weeks in February 1999) was devoted solely to the collection of highest quality tracking data and spacecraft disturbance were minimized. During the mapping phase, MGS was located in a frozen orbit, in order to minimize orbit-to-orbit altitude variations, and the periapsis remained over the South Pole.

Table 4.9 reports the average orbit overlap for the GCO mission phases. With crossovers, we have an average orbit consistency of under a decimeter in radial direction, and 5.7 m in total position. A comparison between the solutions with and without crossovers for this phase reveals that the altimeter crossover data contribute some enhanced sensitivity to the gravity field reconstruction. Even if the change in the calculated value of the gravity anomalies due to addition of the altimeter crossover data is negligible (<0.1 mGal), the orbit tests do provide some evidence that the addition of the MOLA crossovers strengthens the gravity solution, since the total orbit discrepancy is reduced from 12.3 to 5.7 m.

X-band		**Formal uncertainties**		
		X (m)	Y (m)	Z (m)
Batch 1	Without crossover	42.954	20.753	20.214
	With crossover	**42.519**	**20.501**	**19.752**
Batch 2	Without crossover	35.708	19.996	24.753
	With crossover	**34.750**	**19.423**	**23.116**
Batch 3	Without crossover	57.410	11.691	18.439
	With crossover	**45.412**	**9.437**	**13.439**
Batch 4	Without crossover	76.186	54.919	66.975
	With crossover	**47.099**	**33.315**	**38.241**
Batch 5	Without crossover	39.359	116.979	127.340
	With crossover	**25.564**	**77.028**	**84.403**

Table 4.11: Multiarc estimation of the batches (X-band): position formal uncertainties

The overlap comparison for the mapping phase is summarized in table 4.10. The orbit overlap in the radial direction are noticeably higher than for the other mission phase. A number of factors may be responsible for the higher overlaps including longer arc length, less favorable orbit geometry with respect to the Earth line of sight, and more frequently gaps in tracking. Moreover, in these tests, any change due to the addition of crossover data are discernible.

This long review of previous analysis of orbit determination with and without crossovers gives continuitity to our results. By improving the accuracy of radio data (from S, to X and later to Ka band), the contribution of crossover observables in the determination process tends to be drammatically reduced and the abatement of the error in the spacecraft position is also conditioned by other factors, as in the mapping phase of MGS.

As a final case study, we carried out a numerical simulation with the same setup used for BepiColombo, but supposing to have only the X-band link from Cebreros, first with radio tracking data only, and later with radio and crossover observables. Crossover observables are weighted considering an expected RMS of 1 m.

In tables 4.11, 4.12 and 4.13, we summarized the mean formal uncertainties of the spacecraft position obtained for each step of the sequential batch process, as we did for the Ka-band case. Adding crossovers in the orbit determination process allowed an improve-

Multiarc	**Formal uncertainties**		
	X (m)	Y (m)	Z (m)
Without crossover	20.650	10.584	11.389
With crossover	**16.557**	**8.488**	**8.862**

Table 4.12: Complete multiarc estimation (X-band): position formal uncertainties

Last step	**Formal uncertainties**		
	R (m)	T (m)	H (m)
Without crossover	0.110	34.623	36.328
With crossover	**0.104**	**33.820**	**35.968**

Table 4.13: Last step (X-band): position formal uncertainties

ment in the spacecraft positioning from some tens of centimeters, up to several meters. The improvement in the gravity field formal uncertainties is minimal (< 0.7 mGal). These results are in good agreement with what we found in literature.

5

CONCLUSIONS

The work presented here can be considered as the continuation of past analyses, realized in different contexts, but with the common aim to evaluate, and possibly exploit, the contribution of crossover observables in the orbit determination problem. Moreover, we had the objective to assess the optimum criterion to determine Mercury's gravity and topography for the BepiColombo mission.

We will briefly summarize here all what has been done for our study, in order to point out the main aspects and the obtained results.

First of all, a realistic setup of the BepiColombo radio science experiment has been drawn, simulating Doppler and range observables with the extremely high accuracy these measurements can reach thanks to the novel Ka-band transponder, the multifrequency link and tropospheric calibration, and taking into account all the recent modifications in the spacecraft design and mission operations (reaction wheels desaturation maneuvers, occultation periods).

The estimation setup has been then selected, opting for the more complex batch sequential process, instead of a multiarc approach. The main advantage of the batch sequential approach lies in the possibility of consecutive updates of the dynamical model, in order to improve the trajectory reconstruction and to avoid divergence problems, due to forces mismodeling and numerical integration.

Then, a first set of simulations has been realized for computing the attainable accuracies and for verifying that the experiment goals can be reached.

Once the simulation and estimation setup is completed, we started studying the crossovers problem. Those observables are not implemented in the Orbit Determination Program, the JPL software we are using for numerical simulations. It has been therefore necessary to develop several programs for generating and including crossovers in the process.

A first software allows simulating laser altimeter measurements, as radial distance between the spacecraft in the simulated trajectory and the topography of the planet. The added noise has two main contributions: a white Gaussian noise, due to the laser altimeter measurement error, and a linear part, increasing with the spacecraft altitude and due to the nadir pointing error and the mean slope of the planet's surface.

Another program is dedicated to crossovers detection. The ground tracks are divided into colatitude band and the crossover search, carried out within each single area, is speeded up thanks to parallel processing. Linear interpolation and change of sign criterion are used to locate the crossover on the planet surface. The code has been compared with an independently developed software used at DLR, showing difference in crossover location between 50 cm and 1 m on the planet's surface.

Finally the crossover observables must be included in the least square estimation filter software. The code developed in our laboratory has the capability to include new parameters and new observables, but it was able to process only observables with partial derivatives with respect to global parameters and local parameters of a single arc. In a multiarc approach, it can happen that a crossover is formed by two orbits pertaining to two different arcs. Therefore such observable will have partial derivatives with respect to two different set of local parameters.

The least square filter code has been modified, allowing to process new observables depending from global and two set of local parameters. At the same time, another program has been developed for computing crossovers partial derivatives with respect all the solve-for parameters and residuals. In this way, it has been possible to realize an estimation process with the contribution of both radio and crossover observables.

A simplified setup has been used to evaluate crossovers contribution for the BepiColombo radioscience experiment. A reference case with only radio observables has been carried out and used as comparison term. Three different weights of crossover observables have been considered. The results, obtained by comparing the formal uncertainties associated to the spacecraft position components with those obtained in the reference case, show improvements in the spacecraft positioning of few centimeters, when the crossover weighting factor is computed considering an expected residual RMS of 1 m.

Orbit overlap	**R**(m)	**T**(m)	**H**(m)
LRO (GLGM-3)	0.54	35.64	30.35
LRO (LLGM-1)	-0.22	7.07	6.53
MGS (GCO phase)	0.03	6.66	0.29
MGS (mapping phase)	-0.03	0.01	-0.06
Formal uncertainties	**X**(m)	**Y**(m)	**Z**(m)
BC (Ka band)	0.09	0.05	0.05
BC (X band)	4.09	2.10	2.53

Table 5.1: Improvements obtained with crossovers for different missions

Our results have been compared with past analysis of different missions, and it appears evident that the crossover contribution decreases with the increasing of the radio observables accuracy.

In the table 5.1 we summarized our results and past results from the literature. For LRO and MGS cases, where real data have been analyzed, the reported values are the differences between the overlap discrepancies obtained with only radio observables and with both radio and crossovers. For the numerical simulation of BepiColombo, we reported the differences in formal uncertainties. A positive number means an improvement in the determination of that component, thanks to the inclusion of crossover observables in the orbit determination process.

The radio measurements accuracy increases accordingly to the frequency used: S-band for LRO, X-band for MGS and Ka band for BepiColombo (the BepiColombo case with X-band was simply a case-study). On the contrary, the improvements obtained by using crossovers decrease: we have enhancements from several meters to tens of meters for LRO, from few centimeters to some meters for MGS, and of few centimeters for BepiColombo (Ka band).

Consequently, we can state that, with the foreseen accuracy of radio observables, the BepiColombo MPO trajectory can be inferred exclusively from Doppler and range measurements, with an extremely high accuracy. The precise reconstruction of Mercury's surface topography can be carried out in a second step, using laser altimeter measurements.

We demonstrated that the information content of laser altimeter observables (exploited in terms of crossovers) does not improve the trajectory estimation of a quantity sufficient to justify the increase of computational complexity and time needed to include crossovers in the orbit determination process.

A more realistic setup, with desaturation maneuvers, accelerometer noise and other events we did not implement here, could be analyzed, but, at the same time also laser altimeter measurements must be make less ideal. Nadir pointing error and mean surface slope must be taken into account in the computation of additional noise, augmenting significantly the expected crossovers residual RMS. Therefore, crossover observables must be deweighted, vanishing their possible contribution in improving the trajectory reconstruction in a more complex setup.

Finally, we want to clarify that the software developed for BepiColombo radio science experiment scenario is not mission dependent. It can be used to analyze data of past or future missions with an onboard laser altimeter, improving the potentiality of our laboratory.

BIBLIOGRAPHY

Asmar, S., Armstrong, J. W., Iess, L., and Tortora, P. (2005). Spacecraft Doppler tracking: noise budget and accuracy achievable in precision radio science observations. *Radio Science*, 40.

Benkhoff, J., van Casteren, J., Hayakawa, H., Fujimoto, M., Laasko, H., Novara, M., Ferri, P., Middleton, H. R., and Ziethe, R. (2010). BepiColombo - Comprehensive exploration of Mercury: mission overview and science goals. *Planetary and Space Science*, 58:2–20.

Bertotti, B., Comoretto, G., and Iess, L. (1993). Doppler tracking of spacecraft with multi-frequency links. *Astronomy and Astrophysics*, 269:608–616.

Bertotti, B., Farinella, P., and Vokrouhlicky, D. (2003a). *Physics of the Solar System*. Kluwer Academic Publishers.

Bertotti, B., Iess, L., and Tortora, P. (2003b). A test of general relativity using radio links with the Cassini spacecraft. *Nature*, 425:374–376.

Blewett, D. T., Chabot, N. L., Denevi, B. W., Ernst, C. M., Head, J. W., Izenberg, N. R., Murchie, S. L., Solomon, S. C., Nittler, L. R., McCoy, T. J., Xiao, Z., Baker, D. M. H., Fassett, C. I., Braden, S. E., Oberst, J., Scholten, F., Preusker, F., and Hurwitz, D. M. (2011). Hollows on Mercury: MESSENGER Evidence for Geologically Recent Volatile-Related Activity. *Science*, 333:1856–1859.

Burgess, E. (1974). Mariner 10 data reveal Mercury's uniqueness. *New Scientist*, 63:172.

Dunne, J. A. and Burgess, E. (1978). *The voyage of Mariner 10. Mission to Venus and Mercury*. National Aeronautics and Space Administration Scientific and Technical Information Office.

Gardner, C. S. (1992). Ranging performance of satellite laser altimeters. *IEEE Transactions on Geoscience and Remote Sensing*, 30:1061–1072.

Genova, A., Marabucci, M., and Iess, L. (2012). A batch-sequential filter for the BepiColombo radio science experiment. *Journal of Aerospace Engineering, Sciences and Applications*, 4:17–30.

Grard, R. and Balogh, A. (2001). Returns to Mercury: science and mission objectives. *Planetary and Space Science*, 49:1395–1407.

Grard, R., Novara, M., and Scoon, G. (2000). BepiColombo - A multidisciplinary mission to a hot planet. *ESA bulletin*, 103.

Gunderson, K., Thomas, N., and Rohner, M. (2006). A laser altimeter performance model and its application to BELA. *IEEE Transactions on Geoscience and Remote Sensing*, 44:3308–3319.

Iafolla, V. and Nozzoli, S. (2001). Italian Spring Accelerometer (ISA) a high sensitive accelerometer for "BepiColombo" ESA CORNERSTONE. *Planetary and Space Science*, 49:1609–1617.

Iess, L., Asmar, S., and Tortora, P. (2009). MORE: An advanced tracking experiment for the exploration of Mercury with the mission BepiColombo. *Acta Astronautica*, 65:666–675.

Iess, L. and Boscagli, G. (2001). Advanced radio science instrumentation for the mission BepiColombo to Mercury. *Planetary and Space Science*, 49:1597–1608.

Jehn, R. (2012). BepiColombo Mercury Cornerstone Consolidated Report on Mission Analysis (BC-ESC-RP-05500, is.4.1). Technical report, European Space Agency - European Space Operations Centre - Ground Systems Engineering Department.

Koch, C., Kallenbach, R., and Christensen, U. (2010). Mercury's global topography and tidal signal from laser altimetry by using a rectangular grid. *Planetary and Space Science*, 58:2022–2030.

Lemoine, F. G., Smith, D. E., Rowlands, D. D., Zuber, M. T., Neumann, G. A., Chinn, D. S., and Pavlis, D. E. (2001). An improved solution of the gravity field of Mars (GMM-2B) from Mars Global Surveyor. *Journal of Geophysical Research*, 106:23359–23376.

Marabucci, M., Iess, L., and Genova, A. (2010). Numerical Simulations of the Radio Science Experiment of the Mission BepiColombo to Mercury. In *Advance in the astronautical sciences, in proceeding of Space Flight Mechanics*.

Mazarico, E., Lemoine, F. G., Han, S. C., and Smith, D. E. (2010). GLGM-3: a degree-150 lunar gravity model from the historical tracking data of NASA Moon orbiters. *Journal of Geophysical Research*, 115.

Mazarico, E., Rowlands, D. D., Neumann, G. A., Smith, D. E., Torrence, M. H., Lemoine, F. G., and Zuber, M. T. (2011). Orbit determination of the Lunar Reconnaissance Orbiter. *Journal of Geodesy*, 86:193–207.

McNutt, R. L., Solomon, S. C., Grard, R., Novara, M., and Mukai, T. (2004). An international program for Mercury exploration: synergy of MESSENGER and BepiColombo. *Advances in Space Research*, 33:2126–2132.

Milani, A., Rossi, A., Vokrouhlicky, D., Villani, D., and Bonanno, C. (2001). Gravity field and rotation state of Mercury from the BepiColombo Radio Science Experiments. *Planetary and Space Science*, 49:1579–1596.

MORE Team (2011). MORE Science Performance Report (SPR) - BC-MRE-RP-20020. Technical report, ESA document.

Moyer, T. D. (1971). Mathematical formulation of the Douple-Precision Orbit Determination Program (DPODP). Technical report, Jet Propulsion Laboratory, California Institute of Technology, Pasadena, CA.

Neumann, G. A., Zuber, M. T., Wieczorek, M. A., Mc Govern, P., Lemoine, F. G., and Smith, D. (2004). Crustal structure of Mars from gravity and topography. *Journal of Geophysical research*, 109.

Panagiotacoupulos, N. D., Zielenbach, J. W., and Duesing, R. W. (1974). An introduction to JPL's orbit determination program. Technical report, Jet Propulsion Laboratory, National Aeronautics and Space Administration.

Peale, S. J. (2005). The free precession and libration of Mercury. *Icarus*, 178:4–18.

Peale, S. J., Phillips, R. J., Solomon, S. C., Smith, D. E., and Zuber, M. T. (2002). A procedure for determining the nature of Mercury's core. *Meteoritics & Planetary Science*, 37:1269–1283.

Rowlands, D. D., Pavlis, D. E., Lemoine, F. G., Neumann, G. A., and Luthcke, S. B. (1999). The use of laser altimetry in the orbit and attitude determination of Mars Global Surveyor. *Geophysical Research Letters*, 26:1191–1194.

Shirley, D. L. (2003). The Mariner 10 mission to Venus and Mercury. *Acta Astronautica*, 53:375–385.

Shum, C. K., Zhang, B. H., Schutz, B. E., and Tapley, B. D. (1990). Altimeter crossover methods for precision orbit determination and the mapping of geophysical parameters. *The Journal of the Astronautical Sciences*, 38:355–368.

Simone, L., Maffei, M., Gelfusa, D., and Boscagli, G. (2008). On-board DSP techinques for Radio-Science applications. In *Signal Processing for Space Communications*.

Smith, D., Zuber, M. T., Jackson, G. B., Cavanaugh, J. F., Neumann, G. A., Riris, H., Sun, X., Zellar, R. S., Coltharp, C., Connelly, J., Katz, R. B., Kleyner, I., Liiva, P., Matuszeski, A., Mazarico, E., Mc Garry, J., Novo-Gradac, A. M., Ott, M. N., Peters, C., Ramos-Izquierdo, L. A., Ramsey, L., Rowlands, D. D., Schmidt, S., Scott, V., Shaw, G. B., Smith, J. C., Swinski, J. P., Torrence, M. H., Unger, G., Yu, A. W., and Zagwodzki, T. W. (2009). The Lunar Orbiter Laser Altimeter investigation on the Lunar Reconnaissance Orbiter mission. *Space Science Review*, 150:209Ð241.

Smith, D. E., Zuber, M. T., Neumann, G. A., and Lemoine, F. G. (1997). Topography of the Moon from the Clementine lidar. *Journal of Geophysical research*, 102:1591.

Smith, D. E., Zuber, M. T., Phillips, R. J., Solomon, S. C., Hauck, S. A., Lemoine, F. G., Mazarico, E., Neumann, G. A., Peale, S. J., Margot, J. L., Johnson, C. L., Torrence, M. H., Perry, M. E., Rowlands, D. D., Goossens, S., Head, J. W., and Taylor, A. H. (2012). Gravity Field and Internal Structure of Mercury from MESSENGER. *Science*, 336:214–217.

Solomon, S. C., McNutt, R. L., Gold, R. E., Acuña, M. H., Baker, D. N., Boynton, W. V., Chapman, C. R., Cheng, A. F., Gloeckler, G., Head Iii, J. W., Krimigis, S. M., McClintock, W. E., Murchie, S. L., Peale, S. J., Phillips, R. J., Robinson, M. S., Slavin, J. A., Smith, D. E., Strom, R. G., Trombka, J. I., and Zuber, M. T. (2001). The MESSENGER mission to Mercury: scientific objectives and implementation. *Planetary and Space Science*, 49:1445–1465.

Solomon, S. C., McNutt, R. L., Gold, R. E., and Domingue, D. L. (2007). MESSENGER Mission Overview. *Space Science Reviews*, 131:3–39.

Tapley, B., Schutz, B., and Born, G. H. (2004). *Statistical Orbit determination*. Academic Press.

Thomas, N., T., S., Barriot, J.-P., Benz, W., Beutler, G., Christensen, U., Dehant, V., Fallnich, C., Giardini, D., Groussin, O., Gunderson, K., Hauber, E., Hilchenbach, M., Iess, L., Lamy, P., Lara, L.-M., Lognonné, P., Lopez-Moreno, J. J., Michealis, H., Oberst, J., Resendes, D., Reynaud, J.-L., Rodrigo, R., Sasaki, S., Seiferlin, K., Wieczorek, M., and Whitby, J. (2007). The BepiColombo Laser Altimeter (BELA): concept and baseline design. *Planetary and Space Science*, 55:1398–1413.

Tortora, P., Iess, L., Bordi, J., Ekelund, J., and Roth, D. (2004). Precise Cassini navigation during solar conjunction through multifrequency plasma calibrations. *Journal of Guidance, Control, and Dynamics*, 27:251–257.

Zuber, M. T., Smith, D. E., Lehman, D. H., Hoffman, T. L., Asmar, S. W., and Watkins, M. M. (2012). Gravity Recovery and Interior Laboratory (GRAIL): Mapping the Lunar Interior from Crust to Core. *Space Science Review*.